[American Journal of Science, Vol. 320, October, 2020, P. 637–676, DOI 10.2475/10.2020.01]

American Journal of Science

OCTOBER 2020

MIOCENE TO PLEISTOCENE GLACIAL HISTORY OF WEST ANTARCTICA INFERRED FROM NUNATAK GEOMORPHOLOGY AND COSMOGENIC-NUCLIDE MEASUREMENTS ON BEDROCK SURFACES

PERRY SPECTOR*,†, JOHN STONE**, GREG BALCO*, TREVOR HILLEBRAND**,
MIKA THOMPSON**, and TARYN BLACK**

ABSTRACT. We report geomorphic observations and cosmogenic-nuclide measurements on bedrock surfaces from three isolated nunatak groups in West Antarctica: the Pirrit Hills and Nash Hills, located in the Weddell Sea sector, and the Whitmore Mountains, located on the Ross-Weddell divide. The objectives of this paper are to (i) establish a chronology for landscape development at these sites and (ii) quantify the long-term history of ice-thickness variations in West Antarctica. These nunataks display relic alpine landscapes on which weathered bedrock surfaces are superimposed. In the Pirrit Hills, an erosional trimline is etched into alpine ridges and separates smooth-crested ridges below from serrated ridges above. Below the trimline, geomorphic evidence indicates repeated frozen-based ice cover, while above the trimline evidence for ice cover is entirely absent. There is also no geomorphic evidence for thicker-than-present ice at the Whitmore Mountains. Cosmogenic nuclide concentrations in the oldest bedrock surfaces from the Whitmore Mountains and from above the Pirrit Hills trimline indicate uninterrupted exposure for ~12 Myr at extraordinarily low erosion rates. This places a lower limit on the timing of the formation of alpine landscapes in West Antarctica, and we hypothesize that this occurred during the relatively warm climates prior to the mid-Miocene cooling. The absence of evidence for thicker ice at the Whitmore Mountains is consistent with the hypothesis that the divide was typically thinner than present during Pleistocene glacial periods due to reduced accumulation. Bedrock surfaces below the trimline have much lower nuclide concentrations and are most easily explained by a scenario of repeated frozen-based ice cover and occasional subglacial plucking, which is consistent with geomorphic observations. Bedrock surfaces near the modern ice level appear to have been covered more than half of the time, while higher elevation surfaces indicate progressively less cover. The trimline and associated geomorphic features are very similar to a prominent trimline in the Ellsworth Mountains, and we conclude that these are, in fact, part of the same feature. The Ellsworth trimline is hypothesized to have formed during the mid-Miocene cooling and the transition from alpine to continental glaciation, and our results are consistent with this hypothesis.

Key words: Antarctica, West Antarctic Ice Sheet, cosmogenic-nuclide geochemistry, exposure dating, glacial geology, Miocene, Pleistocene

INTRODUCTION

This paper describes geomorphic observations and cosmogenic-nuclide measurements on bedrock surfaces from three groups of isolated nunataks in West Antarctica.

---

* Berkeley Geochronology Center, Berkeley, California, USA
** Department of Earth and Space Sciences, University of Washington, Seattle, Washington, USA
† Corresponding author: pspector@bgc.org

These are the Pirrit and Nash Hills, located midway between the grounding line and the divide in the Weddell Sea sector, and the Whitmore Mountains, located on the divide between the Ross and Weddell Sea sectors. These sites show features such as horns, arêtes, and cirques that are characteristic of alpine glacier erosion but are unrelated to the modern West Antarctic Ice Sheet (WAIS). Superimposed on these landscapes are weathered bedrock surfaces, and, at lower elevations in the Pirrit and Nash Hills, geomorphic evidence for repeated, frozen-based ice cover. Because these sites are some of the only outcropping peaks in central West Antarctica, they provide an opportunity to study multiple aspects of West Antarctic glacial history. Spector and others (2019) reported ice thickness changes at the Pirrit Hills and Whitmore Mountains since the Last Glacial Maximum (LGM), and the purpose of this paper is to extend that history further back in time. Specifically, we aim to (i) establish the chronology of landscape development of West Antarctic nunataks and (ii) quantify the long-term history of ice thickness variations in West Antarctica.

Relic alpine landscapes exist across Antarctica (for example, Mercer, 1963; Denton and others, 1986, 1992; Holmlund and Näslund, 1994), but investigations into when and under what climatic conditions they developed have been mostly limited to the Transantarctic Mountains. In the Dry Valleys region, which has been the focus of extensive landscape research, multiple lines of evidence establish that alpine landforms were carved during and have been preserved since the mid-Miocene (for example, Marchant and Denton, 1996; Sugden and Denton, 2004). In West Antarctica, with the exception of the Antarctic Peninsula, alpine landscapes have only been studied in Marie Byrd Land and the Ellsworth Mountains. In inland Marie Byrd Land, volcanoes with significant cirque development are only found on pre-mid-Miocene edifices (Rocchi and others, 2006), which suggests minimal landscape change since the mid-Miocene. In the Ellsworth Mountains, the age of the alpine landscape has not been established, but etched across the mountains is a prominent erosional trimline (Denton and others, 1992) hypothesized to have been cut during the mid-Miocene climate transition (Sugden and others, 2017). Here, we report geomorphic observations and cosmogenic-nuclide measurements on bedrock surfaces that further constrain the late Cenozoic landscape history in West Antarctica.

The other main purpose of this paper is to establish constraints on pre-LGM ice-thickness variations in West Antarctica. Such constraints remain rare in part because much of the research on past WAIS change has focused on the last deglaciation. As a result, our knowledge of how different glaciological processes affect ice thickness over glacial-interglacial cycles is largely based on reconstructions of WAIS change since the LGM. Spector and others (2019) report exposure-dating results from two of our field sites, the Pirrit Hills and Whitmore Mountains. At the Pirrit Hills, the WAIS reached a highstand ~330 m above the modern ice level while accumulation rates in West Antarctica were at their ice-age minimum, and subsequent thinning coincided with grounding-line retreat downstream in the Weddell Sea. Other exposure dating studies in the Weddell Sea sector have found similar chronologies (Hein and others, 2016; Balco and others, 2016; Bentley and others, 2017), which collectively imply that the primary control on ice thickness at these sites is the position of the ice-sheet margin in the Weddell Sea. In contrast, at the Whitmore Mountains, Spector and others (2019) conclude that the divide was probably no thicker than present during the LGM, but that it likely thickened briefly during the last deglaciation due to increased accumulation rates and subsequently thinned once the dynamic effect of margin retreat became the dominant glaciological process.

Our goal here is to quantify ice thickness changes at these sites using measurements of long-lived cosmogenic nuclides (^{26}Al, ^{10}Be, ^{21}Ne) in bedrock surfaces. In Antarctica, it is common to find geomorphic evidence indicating that weathered bedrock surfaces have been covered by frozen-based or minimally erosive ice in the past. These surfaces are often avoided by exposure-dating studies aimed at chronicling ice retreat during the most recent deglaciation because they have cosmogenic nuclide concentrations that reflect exposure and ice cover over multiple glacial cycles (for example, Bentley and others, 2006). Here, we exploit this feature of polar glaciation to provide quantitative constraints on the long-term history of exposure and ice cover.

FIELD SITES AND GLACIAL GEOLOGY

Pirrit Hills

The Pirrit Hills are located midway between the grounding line and the divide in a slow-flowing portion of the Institute Ice Stream catchment (fig. 1). They consist of a central massif and several small satellite nunataks. The massif and nearby nunataks are composed of a Jurassic granite (Craddock and others, 2017); metasedimentary rocks outcrop at a few minor nunataks located more than 30 km from the massif. The modern ice-sheet surface is highest on the southwest side of the massif, where katabatic winds have deposited a ~5 to 10 km long snow ramp that rises to the saddle between Mt. Tidd and Mt. Goodwin (fig. 2). The surface is lowest on the northeast, lee-side of the massif, where the winds are forced to descend, warm, and become turbulent. Blue-ice ablation zones are found here along with debris that has accumulated in sheets and moraine ridges.

The Pirrit Hills massif consists of a few major and several minor peaks that are linked by catenary arêtes. All of the peaks, some of which form horns, have sheer faces and are buttressed by steep spurs. These features are characteristic of alpine landscapes and indicate that the Pirrit Hills were carved by erosive mountain glaciers. Because such glaciers do not exist at present, the landscape is a relic and is unrelated to the modern ice sheet.

The spurs that buttress the central massif divide what we assume to be cirque basins whose steep headwalls comprise the majority of the exposed rock in the Pirrit Hills and whose floors are concealed below the present-day ice sheet (fig. 2). The only low-relief areas in the Pirrit Hills are two benches located on opposite sides of the massif. One sits directly below the summit of Mt. Axtell (a subsidiary peak of Mt. Tidd; figs. 3A and 3B) at an elevation of 1600 to 1700 m; the other is located on the west buttress of Mt. Goodwin at an elevation of 1700 to 1850 m (figs. 3D and 4). Both benches have low-relief, concave surfaces that are truncated on most sides by cliffs that drop to the ice surface. The Axtell bench is composed of two basins bisected by the ridge of Mt. Axtell, while the Goodwin bench is a single basin. From these observations we interpret the benches to be the floors of former cirques that have been largely cannibalized by the formation of lower-elevation cirques; however, we cannot fully rule out the possibility that the benches are relics of a pre-glacial landscape.

Throughout the Pirrit Hills, ridge crests near the modern ice surface are blunted and typically have smooth longitudinal profiles. In contrast, crests at higher elevations are sharp and in many places feature serrations that range from delicate spires to gendarmes (figs. 3 and 5). This transition occurs at an elevation of roughly 1600 to 1700 m, which approximately coincides with the height of the Axtell and Goodwin benches. Where most conspicuous, we estimate that the transition occurs over a vertical span of around 50 to 100 m. We interpret this transition to delineate an erosional trimline similar to the trimline in the nearby Ellsworth Mountains (Denton and others, 1992), and we describe the relationship between these features in the Discussion section below.

Bedrock surfaces throughout the Pirrit Hills are weathered and show varying degrees of oxidation, case hardening, wind polish, and tafoni development (fig. 6). Surfaces above the trimline typically display the most advanced stages of weathering,

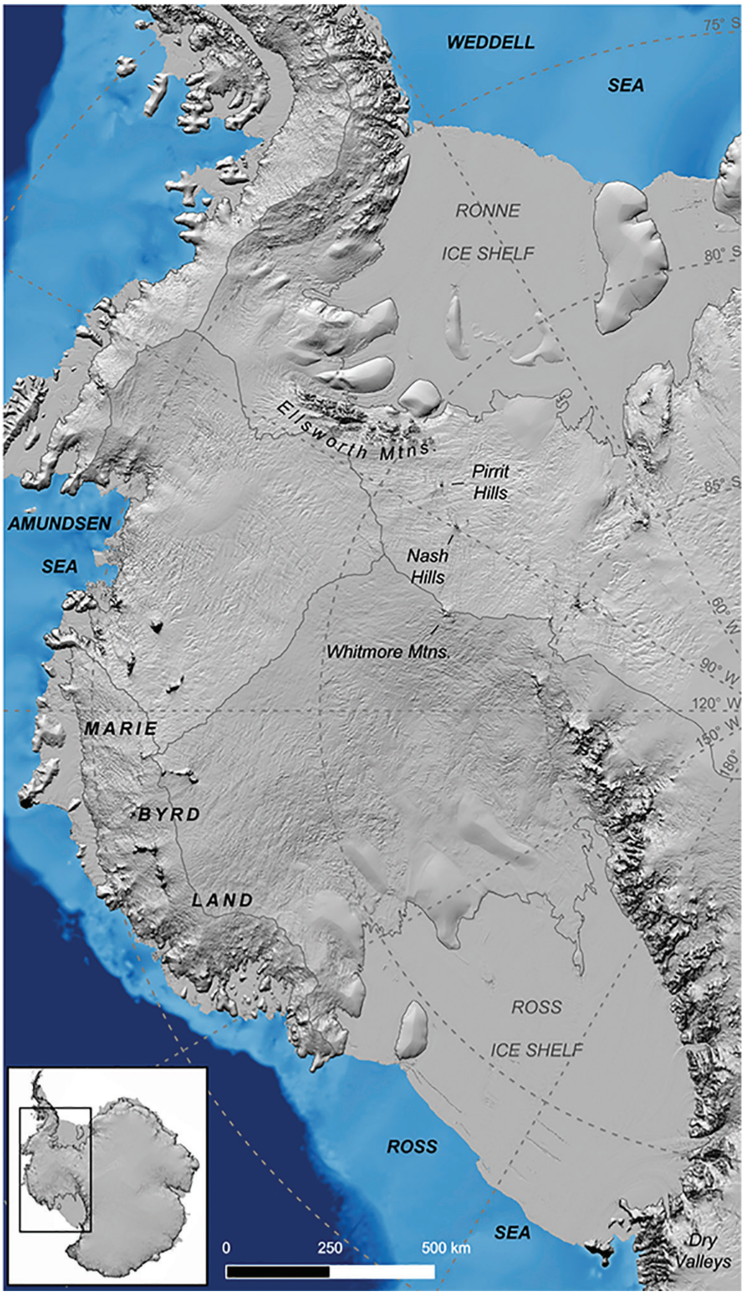

Fig. 1. Map of West Antarctica. Hillshade of ice-sheet surface topography (Howat and others, 2019) is vertically exaggerated 20x and is overlaid on marine bathymetry (Fretwell and others, 2013). The continental shelf is shown in light blue. The grounding line and major ice divides are traced in gray.

but there are many instances of heavily weathered surfaces below, including at the modern ice level where weathered surfaces commonly appear to descend below the surface (fig. 6B). Some of the most weathered surfaces occur on the Axtell and Goodwin benches where the granite is oxidized and exhibits gritty exfoliation sheets,

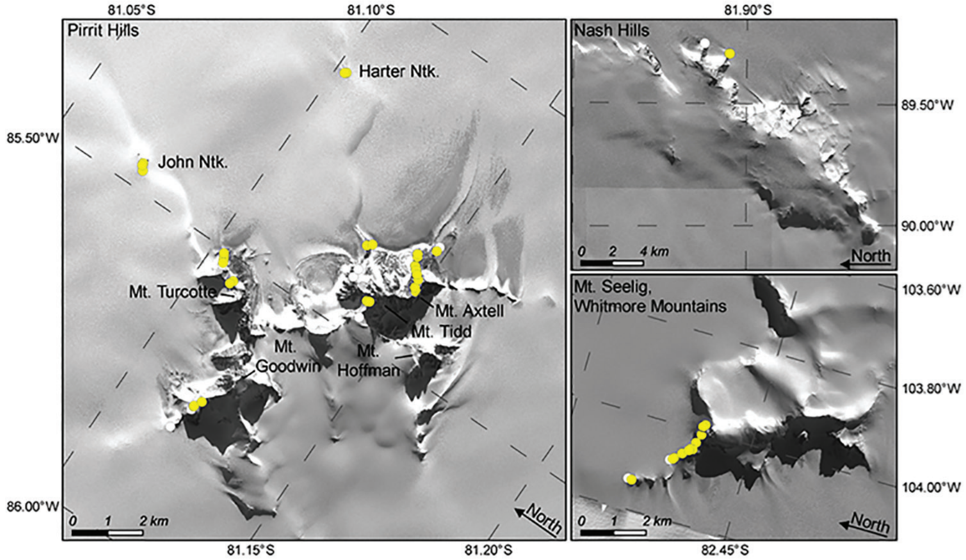

Fig. 2. WorldView satellite imagery © [2020] DigitalGlobe, Inc. of (A) the Pirrit Hills, (B) the Nash Hills, and (C) the Whitmore Mountains. Yellow circles show the locations of bedrock samples. White circles represent bedrock samples that were collected but not analyzed.

case hardening, and delicate tafoni. Grus and/or felsenmeer has accumulated in low-lying areas between joint-bound bedrock blocks that have rounded into knobs and ribs (fig. 4A). Evidence for recent glacial erosion is absent on the Axtell and Goodwin benches or at higher elevations. At lower elevations, there is rare and isolated evidence of erosion, such as anomalously fresh joint surfaces that suggest bedrock slab entrainment by past ice cover (fig. 7).

Glacial deposits are found above the blue-ice ablation zones on the northeast side of the massif. On Mts. Axtell, Tidd, and Turcotte, the depositional limit occurs at a height of ~330 m above the ice sheet, which is just below the Axtell bench and is close to the height of the trimline. We identified glacial deposits by the presence of blunted and broken corners, sub-rounded forms, and fresh to moderately weathered surfaces. Although the bedrock and deposits are both granite, in many cases lithological differences of texture and composition confirmed that the deposits had been transported. Additionally, subsequent analyses revealed that many glacial deposits have significantly higher concentrations of beryl or other beryllium-bearing minerals than bedrock surfaces (see Methods section; fig. A1). The deposits lack evidence of transport by wet-based ice, such as striations or ovoid forms. They show a range of weathering states, ranging from fresh to moderately oxidized and wind polished, but all are considerably less weathered than the bedrock on which they rest. Spector and others (2019) reported exposure ages of these glacial deposits and showed that (i) the WAIS here was at least ~320 m thicker than present during the last ice age, (ii) subsequent thinning occurred mostly after ~14 kyr B.P., (iii) modern ice levels were established within the last ~4 kyr, and (iv) many samples of glacial deposits have pre-LGM ages of up to 1 Myr.

To summarize, we draw the following conclusions about the glacial history of the Pirrit Hills. Across the massif, (i) the trimline, (ii) the height above which only heavily weathered bedrock surfaces are found, and (iii) the depositional limit all occur at similar elevation. This implies that these features are related to the WAIS, rather than the

Fig. 3. Photographs of the Pirrit Hills showing sample locations represented by circles. (A) View from the northeast of Mt. Tidd and Mt. Axtell. The summit of Mt. Axtell is concealed by the two circles. The two ridges below Mt. Axtell (the skyline ridge and the ridge where we collected samples) have smoother crests and profiles than the higher ridge between the Axtell bench and Mt. Tidd. (B) View of Mt. Axtell and the bench from the summit of Mt. Tidd. Labels correspond to sample names in the format "13-NTK-XXX-PRT". Sample 13-NTK-013-PRT was collected from the upper limit of glacial deposits. (C) View to the west of Mt. Turcotte. Labels correspond to sample names in the format "16-PRT-XXXXXXX". (D) Aerial view of Mt. Goodwin from the northwest. The edge of the gently sloping bench is visible on the right side of the image. The bench surface is largely hidden from view. The apparent white skyline on the right is actually the top of low cloud banks. Labels correspond to sample names in the format "16-PRT-XXX-GDW".

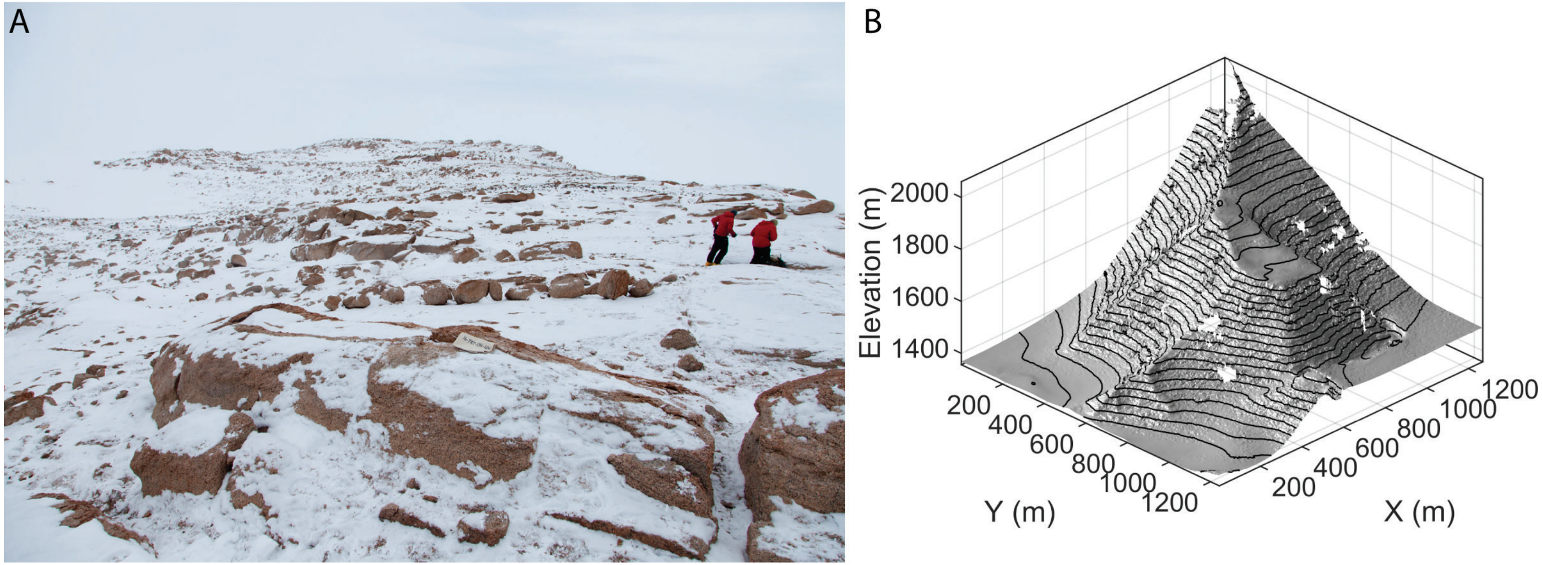

Fig. 4. (A) View of the concave surface of the Goodwin bench looking away from Mt. Goodwin. In the foreground and midground, joint-bound bedrock blocks have been rounded into knobs and ribs. The aligned boulders are tors that are oriented parallel to bedrock joints. (B) Three-dimensional rendering of the relic cirque floor on the west buttress of Mt. Goodwin, derived from a digital elevation model created by the Polar Geospatial Center from DigitalGlobe, Inc. satellite imagery. Contour interval is 20 m.

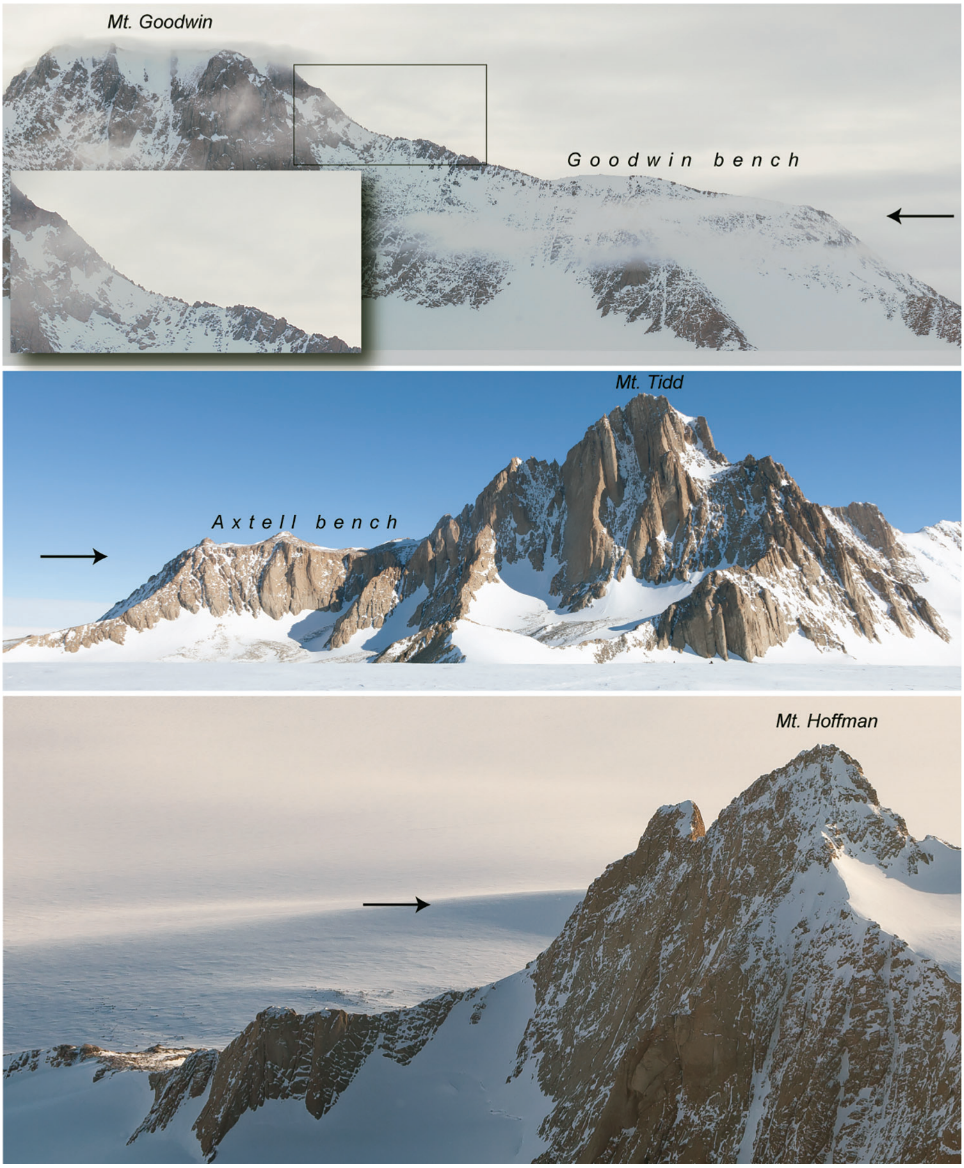

Fig. 5. The trimline at the Pirrit Hills. Top panel: View of Mt. Goodwin from the north. Inset enlarges the area in the rectangle. The trimline is near the slope break below the Goodwin bench (the bench surface is hidden from view). The ridge above the bench is serrated, and the tallest pinnacles are estimated to be 5–7 m tall. The ridge below the bench is smooth. Middle panel: Mts. Tidd and Axtell, viewed from the northeast. The trimline is just below the Axtell bench. The summit and shoulders of Mt. Tidd are castellated, while the low ridges are smooth. Lower panel: Mt. Hoffman, viewed from the summit of Mt. Tidd. The trimline is located below the gendarme. The summit and upper ridge crests are jagged while the lower ridge is blunted. Arrows indicate the approximate trimline height in each image.

mountain glaciers that shaped the landscape. It also suggests that these features are related to each other, and that they mark a level above which has never or rarely been covered by the WAIS. The Axtell and Goodwin benches approximately coincide with the height of the trimline, but because the benches are relatively flat and lack ridges,

Fig. 6. (A) View looking up the steep NE buttress of Mt. Axtell in the Pirrit Hills. The ridge crest is generally a few meters wide. The granite is oxidized and displays evidence of exfoliation in places. In contrast, the glacial deposits, which are visible in the foreground as well as next to the two geologists, are typically only lightly weathered. The depositional limit is near the level of the geologists. (B) Bedrock ridge located to the southeast of Mt. Axtell in the Pirrit Hills. The granite is oxidized and exhibits large cavernous weathering pits (ice axe in foreground for scale). Such weathering features are common at the Pirrit hills, both on higher mountain flanks and intersecting the modern ice surface as shown here.

the trimline is not expressed on the benches themselves. Based on the fact that the benches host some of the most heavily weathered bedrock surfaces in the Pirrit Hills and lack any evidence for past WAIS cover, we infer that they are located just above the height of the trimline. Below the trimline, glacial deposits range from fresh to moderately weathered and have exposure ages that range from Holocene to ~1 Myr (Spector and others, 2019), which implies deposition over multiple ice ages. The absence of striations, polished surfaces, or well-rounded forms, both on deposits and bedrock surfaces establishes that past ice cover was largely frozen to the bed. The presence of weathered bedrock surfaces that intersect and appear to descend below the modern ice-sheet surface (fig. 6B) suggest that the WAIS at the Pirrit Hills has been thinner in the past.

Nash Hills

The Nash Hills are a mostly ice-covered group of mountains that form a southeast-facing escarpment located ~100 km south of the Pirrit Hills (fig. 1). Bedrock ridges project from the escarpment, descend to the present-day ice surface, and bound concave headwalls (figs. 2 and 8A). As for the Pirrit Hills, we interpret such concavities to be cirques whose floors are buried by the present-day WAIS, and we interpret the larger landscape to have been shaped by mountain glaciers that are now absent.

We briefly visited the blunted tips of two ridges shown in figures 2 and 8A. Bedrock surfaces, down to the modern ice level, are weathered and vary from gritty to smooth, resulting from granular exfoliation and wind polishing. Evidence of recent glacial erosion is limited to isolated sites where it appears that an exfoliation slab had been removed (fig. 8B). The more northern of the two spurs adjoins a small ablation zone where glacial debris is accumulating at present. This debris onlaps the tip of the spur and extends at least 60 m above present ice levels (higher elevations were not visited). The debris was not examined in detail, but it appears to be considerably less weathered than the bedrock surfaces on which it rests.

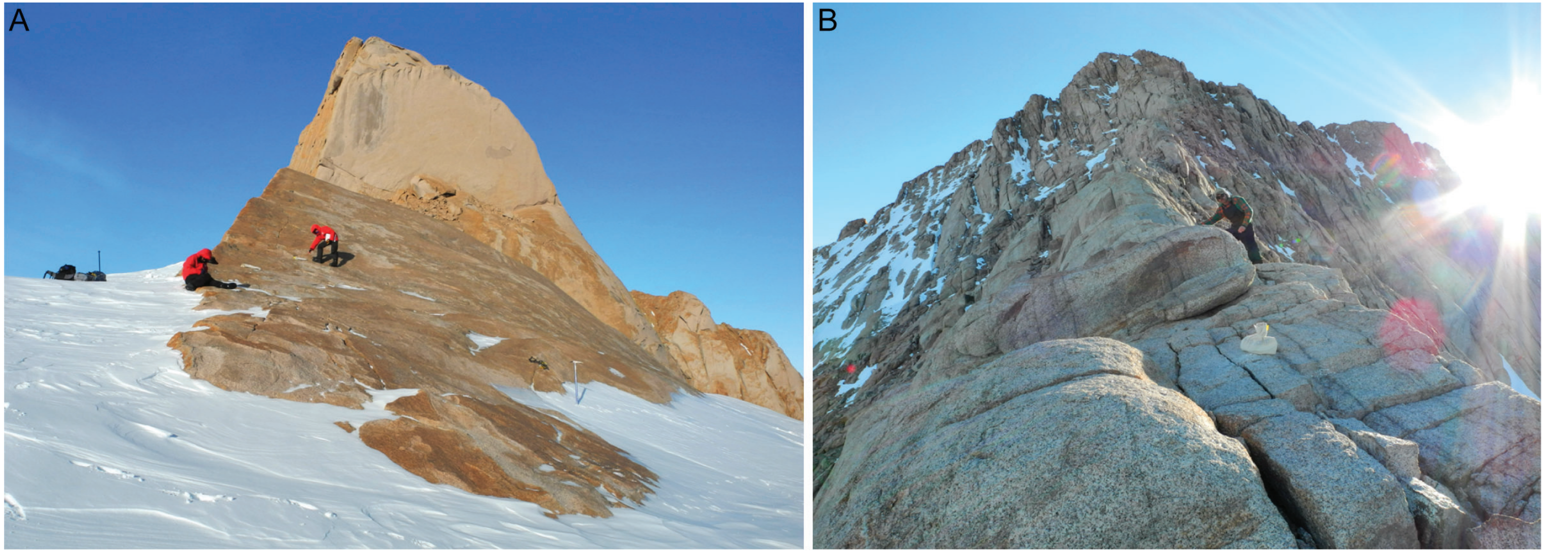

Fig. 7. (A) Photo looking north at the southern tip of John Nunatak in the Pirrit Hills and the location of sample 13-NTK-003-JHN (collected near the person on the right). This is one of the only rounded bedrock surfaces in the Pirrit Hills, and it suggests the possibility of wet-based glaciation. (B) View looking up the northeast ridge of Mt. Axtell. Sample 13-NTK-008-PRT was collected next to the white bag. The area within a few meters of the sample is less weathered than most bedrock surfaces on this ridge. Additionally, it is roughly planar and contiguous with bedrock joints, in contrast to the convex knobs and ribs seen in the foreground and background. These observations suggest removal of a bedrock slab by overriding ice.

Fig. 8. (A) View of the southern of the two spurs visited in the Nash Hills showing approximate sample locations. Numbers correspond to sample names in the format "13-NTK-XXX-NSH". (B) The site at the Nash Hills where sample 13-NTK-032-NSH was collected. The bedrock was sampled next to the rock hammer. The ledge below the sample site is the edge of an exfoliation slab which used to extend and cover sample 13-NTK-032-NSH.

From these observations we conclude that, like the Pirrit Hills, the Nash Hills are a relic alpine landscape whose form is unrelated to the modern WAIS. The absence of wet-based glacial erosion features and the presence of lightly weathered glacial debris indicates cover by frozen-based ice at least once during the late Pleistocene. Based on their proximity and similar glacial geomorphology, we presume that the lower Nash and Pirrit Hills have experienced similar glacial histories. We did not visit high elevations in the Nash Hills, and therefore we do not know whether a trimline similar to that in the Pirrit Hills exists.

Mt. Seelig, Whitmore Mountains

The Whitmore Mountains are a group of peaks located on the divide between the Ross and Weddell Sea sectors of the WAIS (figs. 1 and 2). Although the mountains are mostly snow covered, arêtes and headwalls are exposed above the ice (figs. 2 and 9), indicating that, like the Pirrit and Nash Hills, the Whitmore Mountains were

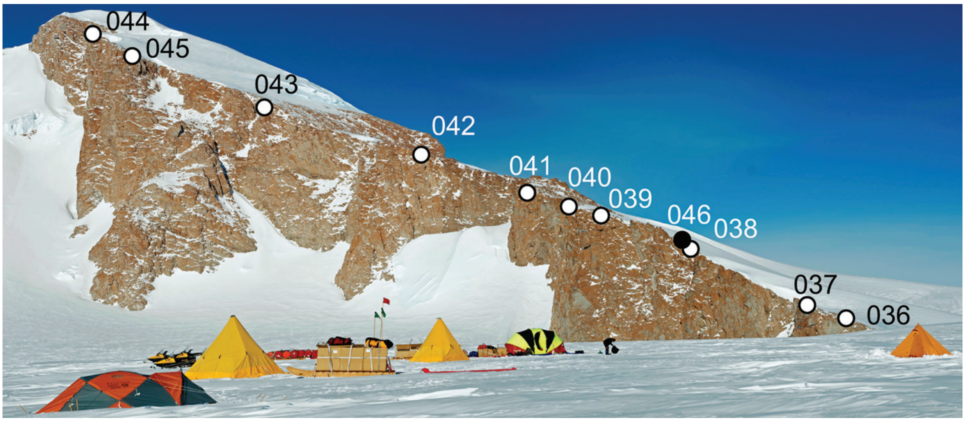

Fig. 9. The northwest ridge of Mt. Seelig, showing sample locations. View is to the south. White circles represent bedrock samples; the black circle represents the till sample. Numbers correspond to sample names in the format "13-NTK-XXX-WHT".

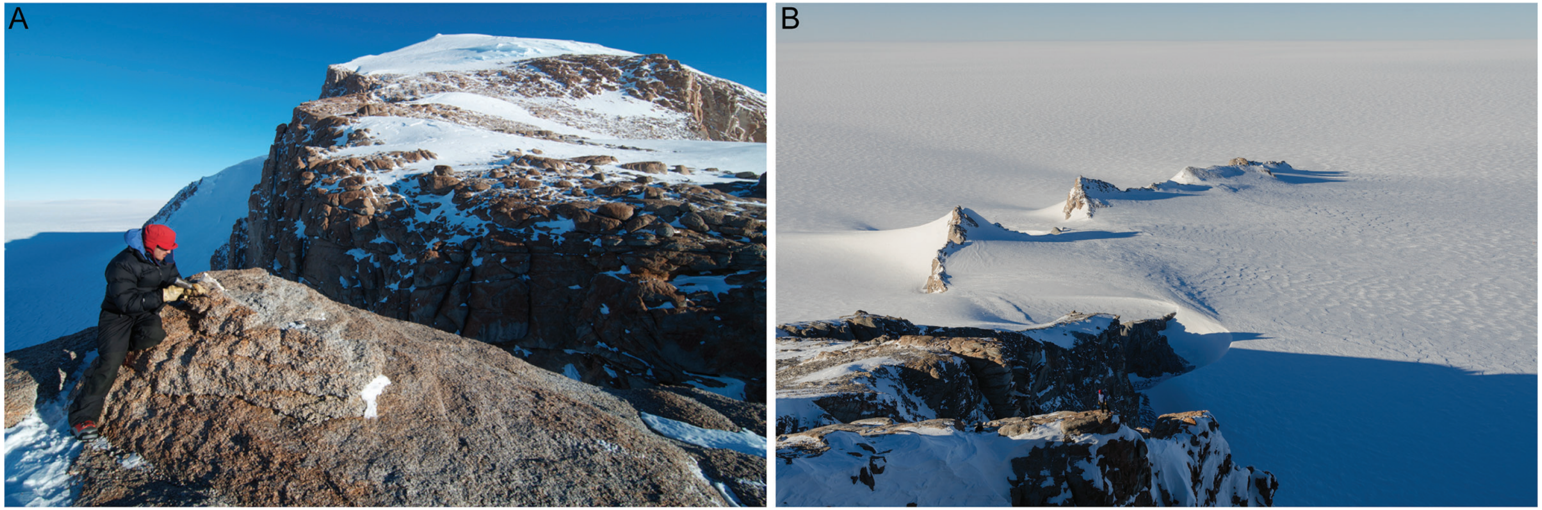

Fig. 10. Left panel shows the view looking up the NW ridge of Mt. Seelig in the Whitmore Mountains. Sample 13-NTK-041-WHT (236 m height) was collected from the bedrock knob in the foreground. The surface has patches of heavy oxidation and has weathered by granular disintegration. The sites of other bedrock samples are visible in the background near the cliff edge. Right panel shows the view looking down the NW ridge of Mt. Seelig. The low, serrated ridge would appear beyond the right edge of the frame of figure 9.

carved by mountain glaciers. We briefly visited the northwest ridge of Mt. Seelig, where heavily weathered bedrock surfaces are superimposed on the alpine landscape. The bedrock surfaces are most akin to surfaces found on the upper flanks of the Pirrit Hills. The granite is oxidized, displaying weathering pits, wind polish, and evidence of granular disintegration (fig. 10). There is no evidence for glacial erosion since the development of the weathered surfaces, nor are there fresh glacial deposits such as those found at the Pirrit and Nash Hills. The absence of fresh glacial deposits is not surprising here at the divide because there is essentially no catchment from which to source debris.

The only visible evidence for past ice cover is a small patch (several square meters) of indurated glacial till found ~150 m above the present ice surface. The till is composed of poorly sorted granite clasts cemented by a matrix of fine-grained material (fig. 11). Some of the cobbles have coarsely smoothed forms. Sparse metasedimentary clasts were also present in the till, and, notably, at least one was striated. Outcrops of metasedimentary rock have been documented elsewhere on Mt. Seelig and in the Whitmore Mountains (Webers and others, 1982), which suggests that the till was derived locally. We interpret these observations to indicate that the till was deposited beneath wet-based ice.

Spector and others (2019) report measurements of cosmogenic ^{14}C in an elevation transect of bedrock samples from Mt. Seelig. These are a subset of the samples on which we have also measured ^{26}Al, ^{10}Be, and ^{21}Ne, discussed below. The ^{14}C concentrations rule out the possibility that the WAIS was more than 190 m thicker than present here during the past 30 kyr. Combined with other constraints from West Antarctica, these data imply that the divide was less than 190 m thicker for a period of less than 8 kyr during the past 15 kyr, which is consistent with the hypothesis that the divide initially thickened due to the deglacial rise in snowfall and subsequently thinned in response to retreat of the ice-sheet margin (Steig and others, 2001).

METHODS

Sample Collection

We collected samples from stable bedrock features displaying evidence for slow subaerial weathering, such as case hardening and oxidation. Where possible, we collected elevation transects of bedrock surfaces (figs. 3, 8A, and 9) in order to identify past highstands and compare exposure and ice cover at different altitudes. We preferentially sampled from windswept ridges and rises where past shielding by cornices, snowfields, *et cetera* is unlikely.

Sample elevations were determined from drift-corrected barometric measurements, bench-marked to a network of geodetic GPS observations. Elevation accuracy is typically 3 to 4 m based on repeat measurements. A vertically oriented fisheye photo was taken at each sample site to measure the degree to which the sample has been shielded from the cosmic-ray flux by the surrounding topography.

Beryllium-10 and Aluminum-26 Measurements

Quartz was separated from crushed rock samples by sieving to 0.25 to 0.5 mm, flotation in heavy liquids, and repeated etching in 2 percent HF. Aluminum and beryllium were extracted from quartz aliquots at the University of Washington Cosmogenic Nuclide Lab. This consisted of addition of ^{9}Be carrier and, for samples with less than 1.5 mg Al, addition of ^{27}Al carrier; HF dissolution; ion exchange chromatography; and precipitation of Be and Al hydroxides (Ditchburn and Whitehead, 1994).

Measurements of total Be by inductively coupled plasma optical emission spectrometry (ICPOES) on aliquots taken after sample dissolution demonstrate that purified quartz separates from bedrock samples from the Pirrit Hills were contaminated

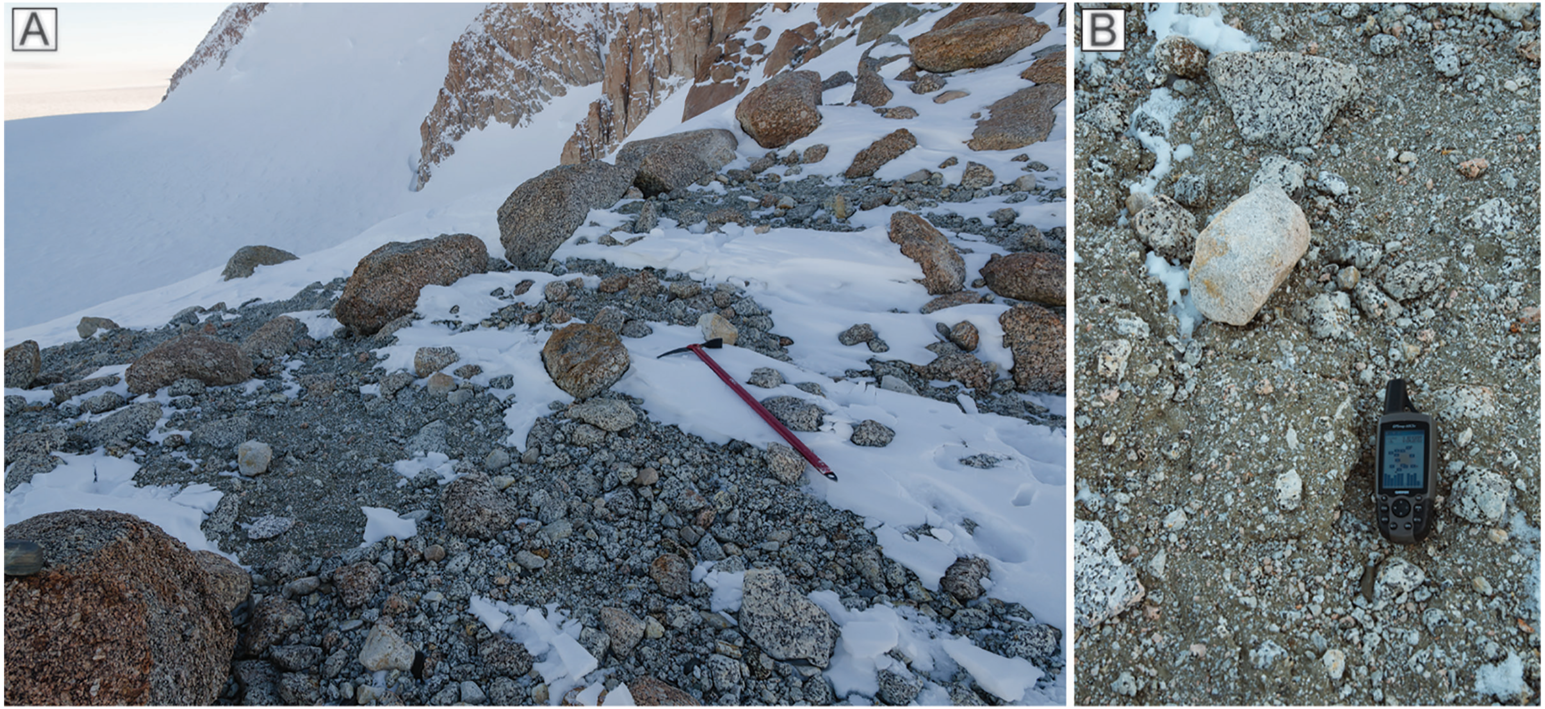

Fig. 11. (A) Photograph of the glacial till from Mt. Seelig. The till is composed of gravel- to cobble-sized clasts cemented by fine-grained material. Although the majority of the clasts are granitic, metasedimentary clasts are also present (not shown). (B) Close up view of the till. The light-colored granite cobble is sample 13-NTK-046-WHT.

with up to 0.004 percent beryl (and/or other Be-bearing minerals) not separated by the procedure described above (fig. A1). Because Be-bearing minerals have HF-solubility that is equal to or lower than that of quartz, they are not removed by etching in dilute HF. Quartz separates from samples of glacial deposits from the Pirrit Hills were also contaminated by Be-bearing minerals (Spector and others, 2019; fig. A1). Because (i) non-carrier Be is measurable at 95 percent confidence in many Pirrit Hills samples and (ii) beryl is a common accessory mineral in Pirrit Hills granite, we calculated ^{10}Be concentrations using ICPOES determinations of total Be rather than the amount of Be added as carrier for all samples from the Pirrit Hills. Although ICPOES results indicate that samples from the Whitmore Mtns. may contain trace non-carrier Be, this is not measurable at 95 percent confidence (fig. A1) and beryl was not observed in any of these samples. Therefore, we calculated ^{10}Be concentrations for these samples, as well as for samples from the Nash Hills, using the amount of Be added as carrier. Concentrations of ^{26}Al were calculated based on ICPOES determinations of total Al for all samples. Any refractory minerals remaining in sample solutions after the initial HF dissolution could dissolve during the subsequent evaporation that occurs at a higher temperature. Therefore, prior to evaporation, all samples were visually inspected, and any grains were removed before proceeding.

Beryllium isotope ratios were measured at the Lawrence Livermore National Laboratory Center for Accelerator Mass Spectrometry (LLNL CAMS). Beryllium isotope ratios were measured relative to the ICN 01-5-4 standard, and ^{10}Be concentrations given in table S1 (http://earth.geology.yale.edu/%7eajs/SupplementaryData/2020/Spector) are calculated relative to a value of $^{10}\text{Be}/^{9}\text{Be} = 2.851 \times 10^{-12}$ (Nishiizumi and others, 2007). Process blanks for all batches were between 4200 ± 1400 and 12700 ± 3500 atoms ^{10}Be, which, for all samples, represents less than 0.26 percent of the total number of atoms present.

Uncertainties in ^{10}Be concentrations (table S1) represent all known sources of laboratory uncertainty combined in quadrature. For sample names prefixed "13-NTK" that were analyzed at LLNL CAMS between 2011 and 2015, we have increased their Be isotope ratio uncertainty above that reported by LLNL CAMS. The larger uncertainties are based on analyses of isotope ratio standards (Nishiizumi and others, 2007) prepared at the University of Washington (UW) and analyzed along with samples. Between 2011 and 2015, these UW standards commonly showed more scatter in isotope ratio than the internal LLNL CAMS standards. To assess this additional source of isotope ratio error, we determined the additional percentage error required to bring the chi-square of the UW standards to 1.0. In the case of the 13-NTK samples, this additional error of 4.8 percent, based on seven standard analyses, has been added in quadrature to the isotope ratio error reported by LLNL CAMS. Bias in the ratios of the UW standards run with the 13-NTK samples was $-2.4\% +/- 3.9\%$, and, because the scatter exceeds the bias, no correction has been applied to the isotope ratios and resulting concentrations in table S1 (http://earth.geology.yale.edu/%7eajs/SupplementaryData/2020/Spector). Samples analyzed at LLNL CAMS after 2015 were not afflicted by this issue.

Aluminum isotope ratios were measured at LLNL CAMS, with the exception of samples 13-NTK-044-WHT and 13-NTK-045-WHT, which were measured at the Purdue Rare Isotope Measurement Laboratory (PRIME Lab). Al isotope ratios were measured relative to the 01-4-2 standard, assuming a nominal $^{26}\text{Al}/\text{Al}$ value of 3.096×10^{-11} (Nishiizumi, 2004).

Neon-21 Measurements

Analytical methods.—Neon isotope measurements at the Berkeley Geochronology Center (BGC) utilized the BGC "Ohio" system, a MAP-215 sector field mass spectrometer with modern ion-counting electronics coupled to a fully automated gas extraction system. Gases were extracted from aliquots of the same purified quartz used for ^{10}Be and ^{26}Al analysis by encapsulating ~150 mg of quartz in a tantalum packet and heating it under vacuum with a 150 W, 810 nm laser diode. Temperature control employed an optical pyrometer coaxial with the laser focusing optics and coupled to a Watlow PID controller. Gases were extracted in either three heating steps at 400°, 850°, and 1100 °C or two heating steps at 800° and 1100°. Extracted gases were reacted with two SAES getters and Ne was frozen to activated charcoal at 33 K. Non-adsorbed gases were pumped away, and Ne was released into the mass spectrometer at 75 K.

Neon isotopes were measured by ion counting on masses 20, 21, and 22 using a Channeltron-type multiplier. Signals on masses 20 and 22 were corrected for interferences from $^{40}Ar^{++}$ and CO_2^{++}, respectively, using a ^{39}Ar spike as described by Balco and Shuster (2009). Absolute calibration of Ne abundance was made by peak height comparison against aliquots of an air standard containing between 5×10^{-16} and 2×10^{-14} mol Ne, processed in the same way as the samples and analyzed several times daily. Neon sensitivity was linear within this range for all samples. Corrections for mass discrimination, when necessary, are also based on the air standard. Volume calibration of the pipette systems and measurement of the pressure of the air standards during loading employed several reference volumes and Baratron capacitance manometers. Measurements of interlaboratory comparison standards (Vermeesch and others, 2015) during the period in which the analyses described in this paper were carried out yielded: 316.3 ± 6 Matoms g^{-1} excess ^{21}Ne for aliquots of CRONUS-A measured in 2014 (mean and standard deviation of 6 measurements); 347.7 ± 9.6 Matoms g^{-1} for aliquots of CREU-1 measured in 2014 (n = 2); and 318.7 ± 10.3 Matoms g^{-1} for aliquots of CRONUS-A measured in 2018 (n = 8). These are indistinguishable from accepted values of 320 Matoms g^{-1} for CRONUS-A and 348 Matoms g^{-1} for CREU-1 (Vermeesch and others, 2015).

Neon isotope compositions and the slope of the neon atmospheric-cosmogenic mixing line for quartz.—Here we describe an improved estimate of the slope of the neon atmospheric-cosmogenic mixing line for quartz. Although this is peripheral to the primary points of this paper, it is nevertheless important for neon isotope systematics.

With the exception of samples from Harter Nunatak (discussed below), all samples have neon isotope compositions that are consistent at 95 percent confidence with two-component mixing of atmospheric and cosmogenic neon (fig. 12).

Samples from the Whitmore Mountains are collinear on a neon three-isotope diagram (fig. 12), and some of them have significantly higher ratios of cosmogenic to atmospheric neon than any other samples that we are aware of. These two features make these samples particularly well suited for estimating the slope of the atmospheric-cosmogenic mixing line. The slope of the mixing line represents the relative rates of spallation production of cosmogenic ^{20}Ne, ^{21}Ne, and ^{22}Ne through the general reaction Si(n, 4p xn)Ne (Niedermann and others, 1993). For quartz, the mixing line slope has been estimated experimentally to be 1.120 ± 0.021 (Niedermann and others, 1993), 1.10 (+0.05, −0.03) (Bruno and others, 1997), 1.10 ± 0.10 (Phillips and others, 1998), 1.143 ± 0.038 (Schäfer and others, 1999), and 1.108 ± 0.014 (2 sigma) (Vermeesch and others, 2015). These estimates were all based on samples with much lower ratios of cosmogenic to atmospheric neon than samples from the Whitmore Mountains (for reference, the maximum $^{21}Ne/^{20}Ne$ ratio measured in these prior studies was around 0.2).

We estimate the slope of the mixing line using the lowest-temperature (425 °C) heating-step data from the Whitmore Mountains (fig. 13), which have the highest cosmogenic-atmospheric ratios of all heating steps (see also Hetzel and others, 2002).

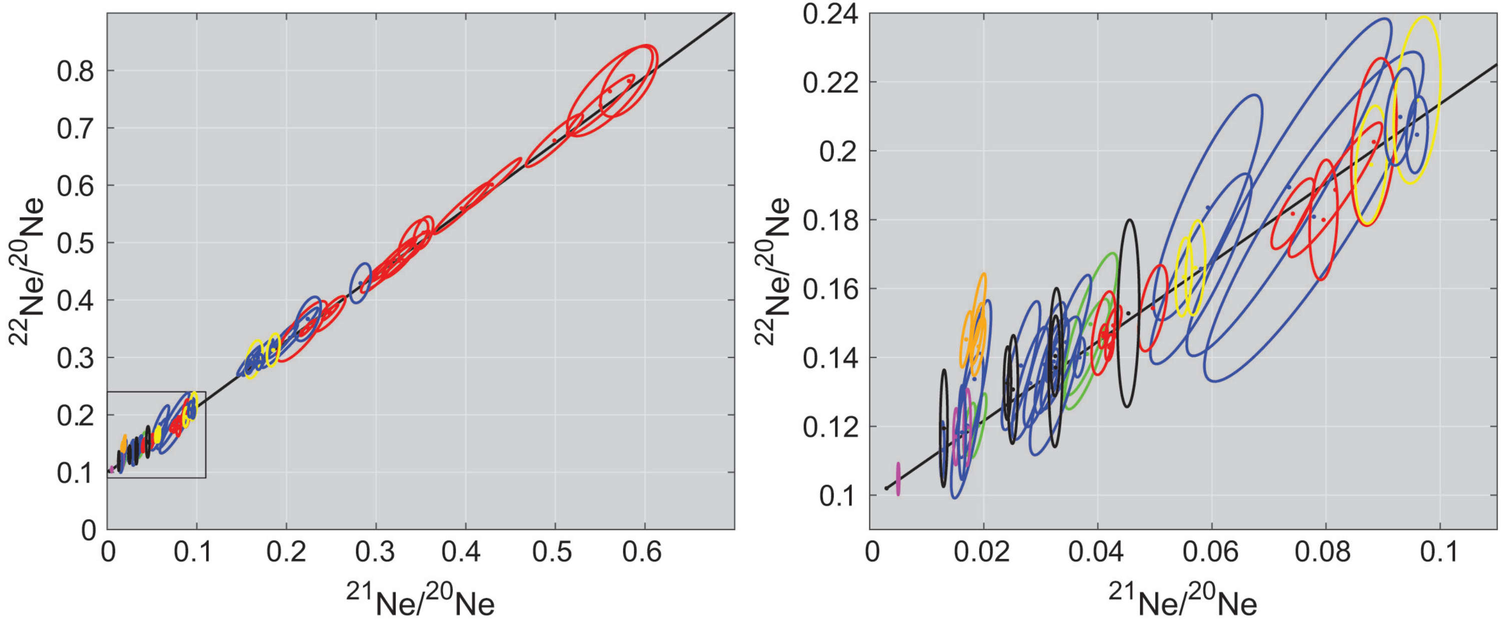

Fig. 12. Neon three-isotope diagram for samples from the Whitmore Mountains (red), Nash Hills (magenta), Mts Tidd and Axtell (blue), Harter Nunatak (orange), John Nunatak (green), Mt. Goodwin (yellow), Mt. Turcotte (black). Ellipses represent 95% confidence regions. The black line is the atmospheric-cosmogenic mixing line determined from samples from the Whitmore Mountains (see discussion in text). The black dot at the left end of the mixing line represents the neon isotope composition of the modern atmosphere. The right panel enlarges the region within the black box in the left panel.

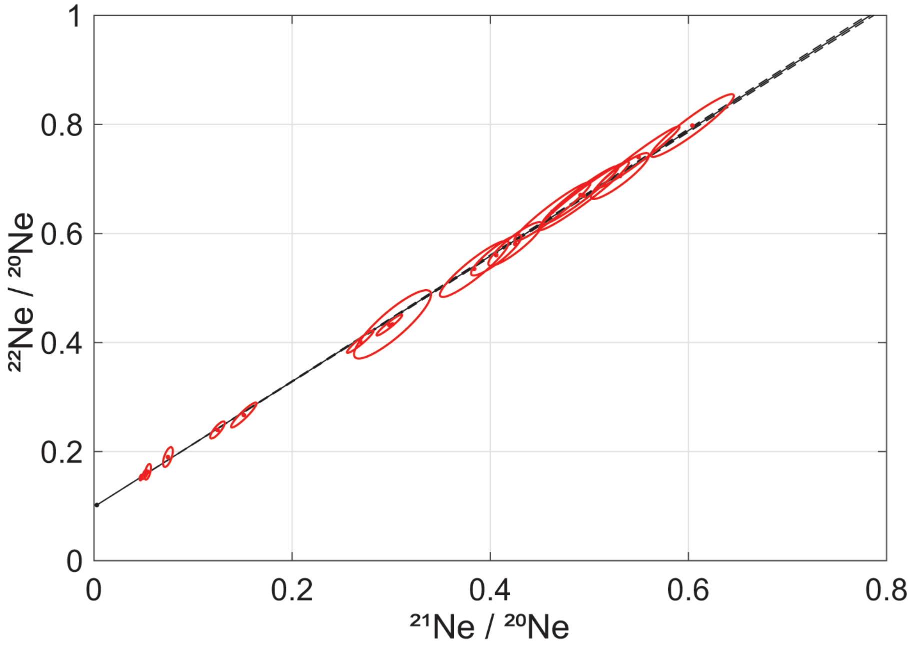

Fig. 13. Neon three-isotope diagram showing 425 °C extraction temperature data for samples from the Whitmore Mountains. Ellipses represent 95% confidence regions. These data are used to estimate the slope and associated uncertainty of the atmospheric-cosmogenic mixing line, represented by the black line and surrounding dashed lines, respectively.

Higher-temperature heating steps are also more likely than lower-temperature steps to extract “trapped” neon with non-atmospheric isotope ratios if such a component exists. Regression of the 425 °C heating-step data via a 1000-iteration Monte Carlo simulation indicates that the slope of the mixing line is 1.150 ± 0.005 (1 standard deviation). This estimate is slightly higher than previous estimates (see above), but within uncertainty of the estimates of Bruno and others (1997), Phillips and others (1998), and Schäfer and others (1999).

Estimation of cosmogenic and nucleogenic ^{21}Ne.—In addition to atmospheric and cosmogenic neon, our samples contain nucleogenic ^{21}Ne and ^{22}Ne produced by alpha-capture reactions on F and O, respectively (NB: fluorite is an accessory mineral in some samples of Pirrit Hills granite) (Niedermann and others, 1993; Niedermann, 2002). Nucleogenic neon has accumulated in quartz samples since they cooled below the neon-in-quartz closure temperature of ~95 °C (Shuster and Farley, 2005), at rates governed by the U and Th concentrations in quartz. The best estimate of the neon-in-quartz closure age of our samples comes from apatite fission-track measurements on samples from the Ellsworth Mtns. (Fitzgerald and Stump, 1991) and from the Whitmore Mtns (Fitzgerald, *personal communication*), which indicate that samples at elevations of 1200 to 1800 m (the elevation range of the samples we report here) cooled below ~110°C around 120 to 140 Myr ago.

We estimate nucleogenic ^{21}Ne concentrations in our samples using this estimate of the neon-in-quartz cooling age and measurements of ^{21}Ne, U, and Th made on an 8 m long bedrock core recovered from the subglacial extension of Harter Nunatak (Spector and others, 2018; Stone and others, 2019). The core site is located around 350 to 400 m from the Harter Nunatak bedrock samples that we report here, but it is at least several kilometers away from the next nearest samples from the Pirrit Hills. Analyses of the core and the overlying basal ice, which will be described in a forthcoming publication, demonstrate that the core site was briefly exposed sometime in the past but has remained continuously ice-covered for at least the past 2.5 Myr (Stone and others, 2019). Measurements of ^{21}Ne excess, which is the sum of all non-atmospheric composition neon, are scattered and show no obvious relationship with depth in the core, indicating significant and highly variable nucleogenic ^{21}Ne.

As mentioned above, samples from Harter Nunatak lie significantly above the atmospheric-cosmogenic mixing line (orange ellipses in fig. 12), which indicates the presence of significant nucleogenic ^{22}Ne (and presumably nucleogenic ^{21}Ne as well). For these samples, we assume that (i) they have the same nucleogenic ^{21}Ne concentration as samples in the core, and (ii) all of the ^{21}Ne below a depth of 2 m in the core, where spallation-produced ^{21}Ne will be minimal, is, in fact, nucleogenic. Hence, we estimate cosmogenic ^{21}Ne in Harter Nunatak samples as the difference between ^{21}Ne excess in the samples and ^{21}Ne excess measured below 2 m in the core, which has a mean of 15.6 Matoms g^{-1}. We increase the ^{21}Ne error in these samples by adding the standard deviation (6.7 Matoms g^{-1}) of the core samples in quadrature.

All other samples that we report here were collected at significant distance from the subglacial bedrock core site, and thus may contain nucleogenic ^{21}Ne concentrations that are different from the core. None of the samples show obvious ^{22}Ne enrichment (fig. 12), which suggests that they have smaller nucleogenic ^{21}Ne components than the samples from Harter Nunatak. Therefore, we consider the ^{21}Ne measured below 2 m in the core to be an upper limit on nucleogenic ^{21}Ne in these samples. We estimate an approximate lower limit on nucleogenic ^{21}Ne in these samples by forward modeling the nucleogenic ^{21}Ne that has accumulated since the rocks cooled below the neon-in-quartz closure temperature. We use the method of Balco and others (2019) and calculate nucleogenic ^{21}Ne produced via the $^{18}O(\alpha,n)^{21}Ne$ reaction as a function of the closure age and the U and Th concentration in quartz. We assume a neon-in-quartz closure age of 120 Myr (see discussion above), and we use the lowest effective U concentration—which approximates total alpha production from U and Th and is defined as $[U] + 0.235[Th]$—measured in the subglacial core of 0.06 ppm. This results in a lower limit on nucleogenic ^{21}Ne of 1.0 Matoms g^{-1}. We estimate nucleogenic ^{21}Ne in all samples not from Harter Nunatak to be 8.3 ± 7.3 Matoms g^{-1}, which represents the mean and range of the estimates from the subglacial core and from the forward calculation described above. This correction represents up to 14 percent of ^{21}Ne excess for samples collected near the present-day ice surface at the Pirrit and Nash Hills, with the exception of one sample, for which the correction represents 24 percent of ^{21}Ne excess. The correction is negligible for high elevation samples from the Whitmore Mountains and Pirrit Hills.

Production Rate Calculations

We compute nuclide production rates using the method of Lifton and others (2014) and Lifton (2016), which is based on models of cosmic-ray fluxes in the atmosphere. As described below, we calibrate spallation production rates for ^{10}Be and ^{26}Al locally using samples from the Whitmore Mountains and Pirrit Hills that are saturated with respect to ^{10}Be and ^{26}Al. Atmospheric pressure at sample sites is calculated using the relation between elevation and Antarctic atmospheric pressure of Stone (2000). Production rates for ^{21}Ne are calculated using the $^{21}Ne/^{10}Be$ production-rate ratio of Balco and others (2019). Production by muons is calculated using the method of Balco (2017). Muon interaction cross sections for ^{21}Ne are from Fernandez-Mosquera and others (2010).

Radionuclide concentrations saturate when the production rate and the decay rate are balanced, which, for ^{26}Al and ^{10}Be, can only occur in samples that have experienced prolonged exposure and negligible erosion. In non-eroding rock surfaces, radionuclide concentrations reach 98% of saturation in a period of time equal to $4/\lambda$, where λ is the decay constant for ^{26}Al or ^{10}Be, which corresponds to 4.1 and 8.0 Myr for ^{26}Al and ^{10}Be, respectively. Production rates based on published calibration datasets (for example Borchers and others, 2016) cause ^{10}Be concentrations of several of the bedrock samples from the Whitmore Mountains and the Pirrit Hills to (i) exceed ^{10}Be saturation concentrations and (ii) have ^{26}Al/^{10}Be ratios that are slightly too low for samples at saturation. On a two-isotope plot, this means that these samples lie to the right of and below the endpoint of the simple-exposure and steady-erosion lines (fig. A2), which is not physically possible if production rates have been accurately estimated. Although low ^{26}Al/^{10}Be ratios are usually consistent with past ice cover, such a scenario is unlikely given that these samples are at or near saturation with respect to ^{26}Al and ^{10}Be, and they exhibit no geomorphic evidence for prolonged ice cover, as discussed above.

Beryllium-10 concentrations in excess of saturation concentrations imply that we are underestimating ^{10}Be production rates. This could be due to multiple factors, including (i) the possibility that these samples have decreased in elevation over time due to changes in glacial isostasy, local tectonics, or mantle dynamics; (ii) the possibility that production rates over the past ~20 kyr—the time period that most production-rate calibration samples are sensitive to (Borchers and others, 2016)—may not be representative of production rates over the past several million years; or (iii) the possibility that there are errors or biases in production-rate scaling models. Establishing why ^{10}Be production rates are underestimated is beyond the scope of this paper; here we focus on long-term ice-thickness variations in West Antarctica and the age of nunatak landscapes.

To remove the potential effects of bedrock elevation change or errors in production-rate scaling models, we calibrate ^{10}Be and ^{26}Al production rates locally by assuming that four samples from the Whitmore Mountains with extremely high nuclide concentrations (13-NTK-037-WHT, 13-NTK-042-WHT, 13-NTK-043-WHT, and 13-NTK-045-WHT) are, in fact, saturated with respect to ^{26}Al and ^{10}Be. Calculating apparent ^{21}Ne exposure ages by (i) assuming zero erosion, (ii) basing production rates on calibration data of Borchers and others (2016), and (iii) using a total ^{21}Ne/^{10}Be production ratio of 4.03 (Balco and others, 2019) results in exposure ages for these samples in the range of around 8 to 12 Myr. Such ages are sufficiently old to be consistent with the idea that these samples are saturated with respect to ^{26}Al and ^{10}Be. After calibrating ^{26}Al and ^{10}Be production rates, we also update ^{21}Ne production rates using a total ^{21}Ne/^{10}Be production ratio of 4.03 (Balco and others, 2019). This calibration procedure results in ^{10}Be and ^{21}Ne production rates that are around 2 percent higher than those predicted by the calibration data of Borchers and others (2016) and ^{26}Al production rates that are around 5 percent lower.

COSMOGENIC NUCLIDE RESULTS

Here, we place quantitative constraints on the age of nunatak landscapes and on long-term ice thickness variations. To do this, we first identify the subset of bedrock samples that record the longest histories of exposure and ice cover. Next, for samples from the Whitmore Mountains and from above the Pirrit Hills trimline where there is no evidence for past ice-sheet cover, we compute exposure ages and erosion rates from ^{26}Al, ^{10}Be, and ^{21}Ne data assuming uninterrupted exposure and steady erosion. For all other samples that have been repeatedly ice-covered in the past, we develop a

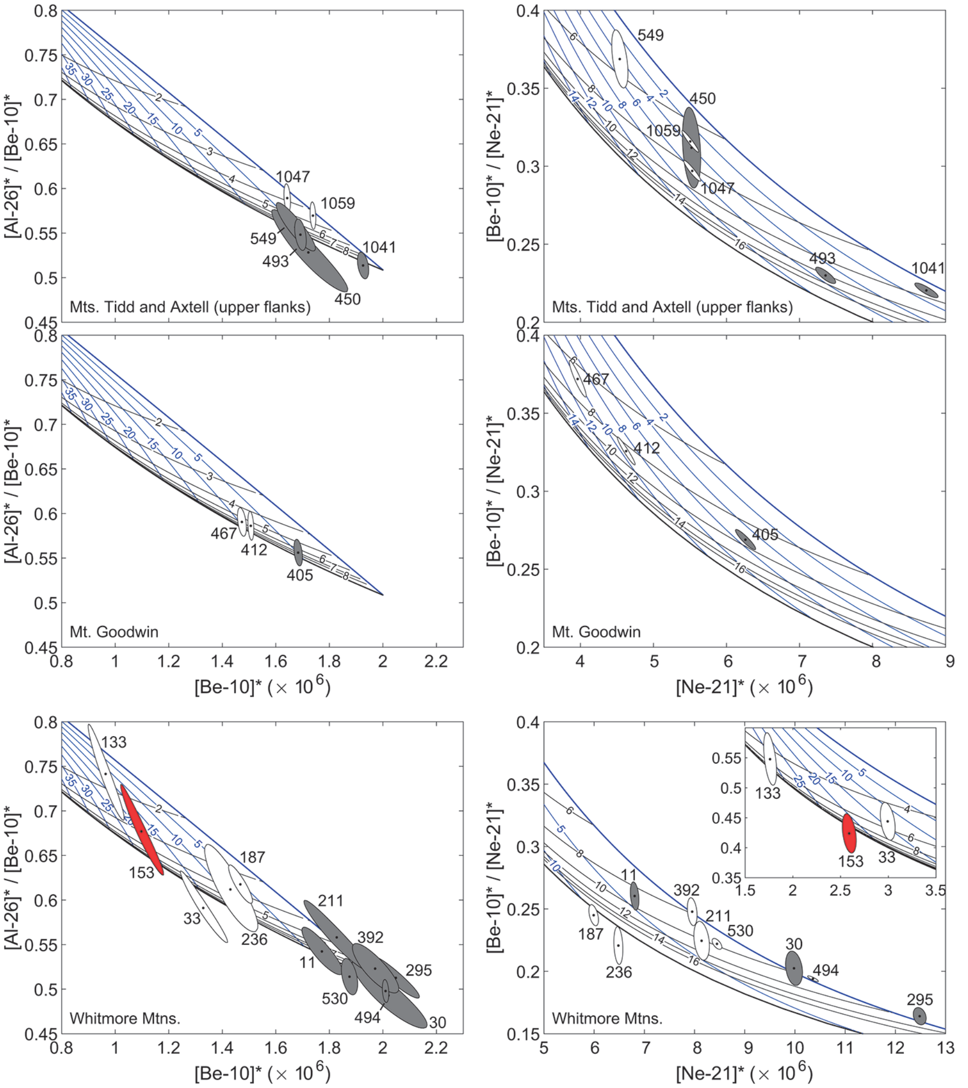

Fig. 14. ^{26}Al-^{10}Be (left) and ^{10}Be-^{21}Ne (right) diagrams for sites in the Pirrit Hills and Whitmore Mountains where geomorphic and cosmogenic-nuclide evidence indicates prolonged and continuous exposure. Nuclide concentrations are normalized to the surface production rate for each sample ($N^*=N/P$, where N is the nuclide concentration and P is the local production rate), to remove the effect of differences in altitude, latitude, shielding, et cetera between samples. Note that the abscissa in the right-hand diagrams is equivalent to the apparent ^{21}Ne exposure age. Ellipses represent 68% confidence regions and are labeled with sample height above the modern ice surface. All data are for bedrock surfaces except for the till from the Whitmore Mountains, which is shown in red. White ellipses represent samples identified as eroded (see main text). Nuclide concentrations of continuously-exposed and non-eroding samples will lie along the upper blue line—the "simple-exposure line". Nuclide concentrations of samples that have reached production-decay-erosion equilibrium will plot along the lower black line—the "steady-erosion line". These lines bound the "simple-exposure region". Blue lines are contours of steady erosion (units: cm Myr^{-1}), and black lines are contours of constant exposure (units: Myr).

model of periodic exposure and ice cover that is consistent with geomorphic observations and explains the measured cosmogenic-nuclide concentrations.

Normalized nuclide concentrations and interpretations of these data appear in figures 14, 15, 16, 17, 18, and 19. Note that we use the term "apparent exposure age"

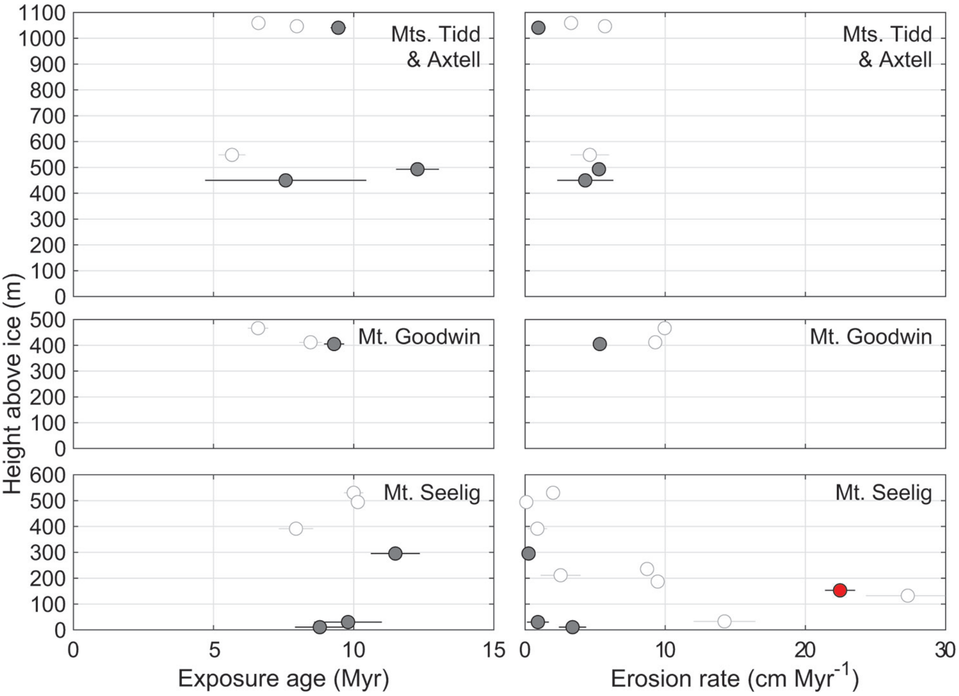

Fig. 15. Exposure ages and erosion rates calculated by solving the system of Equations 1-3 for bedrock samples from above the Pirrit Hills trimline and from the Whitmore Mountains. White circles represent samples identified as having been eroded (see main text). The red circle represents the Whitmore till. Exposure ages calculated for samples whose nuclide concentrations significantly overlap or lie below the steady-erosion line on a two-nuclide diagram (fig. 14) are not meaningful and are thus not shown here.

to refer to the minimum cumulative exposure duration calculated assuming zero erosion. Sample information and nuclide concentrations are reported in table S1 and are archived online in the ICE-D:ANTARCTICA database (http://antarctica.ice-d.org/). Step-degassing results for ^{21}Ne are reported in tables S2-4 (http://earth.geology.yale.edu/%7eajs/SupplementaryData/2020/Spector).

Identification of Samples that Preserve the Greatest Information About Long-Term Exposure and Ice Cover

Because the goal of this paper is to investigate the long-term glacial history, we want to base interpretations on the subset of bedrock samples that record the longest histories of exposure and ice cover. Despite our strategy of sampling weathered bedrock surfaces from stable landforms, as described above, several samples were collected from sites that appear to have been glacially eroded, likely within the past few glacial cycles. Although some high elevation samples have probably never been ice-covered, they have nevertheless experienced different subaerial erosion rates due to wind exposure, friability, or other factors. Here we describe a procedure for identifying samples that record detectable subglacial and/or subaerial erosion so that they can be removed from further consideration.

We first assume that all samples have experienced negligible erosion. For formerly ice-covered samples, this predicts that exposure ages monotonically increase with elevation because of the geometric constraint that a higher-elevation sample cannot be covered by the ice sheet without all lower-elevation samples also being covered. For continuously exposed samples, negligible erosion predicts exposure ages that are

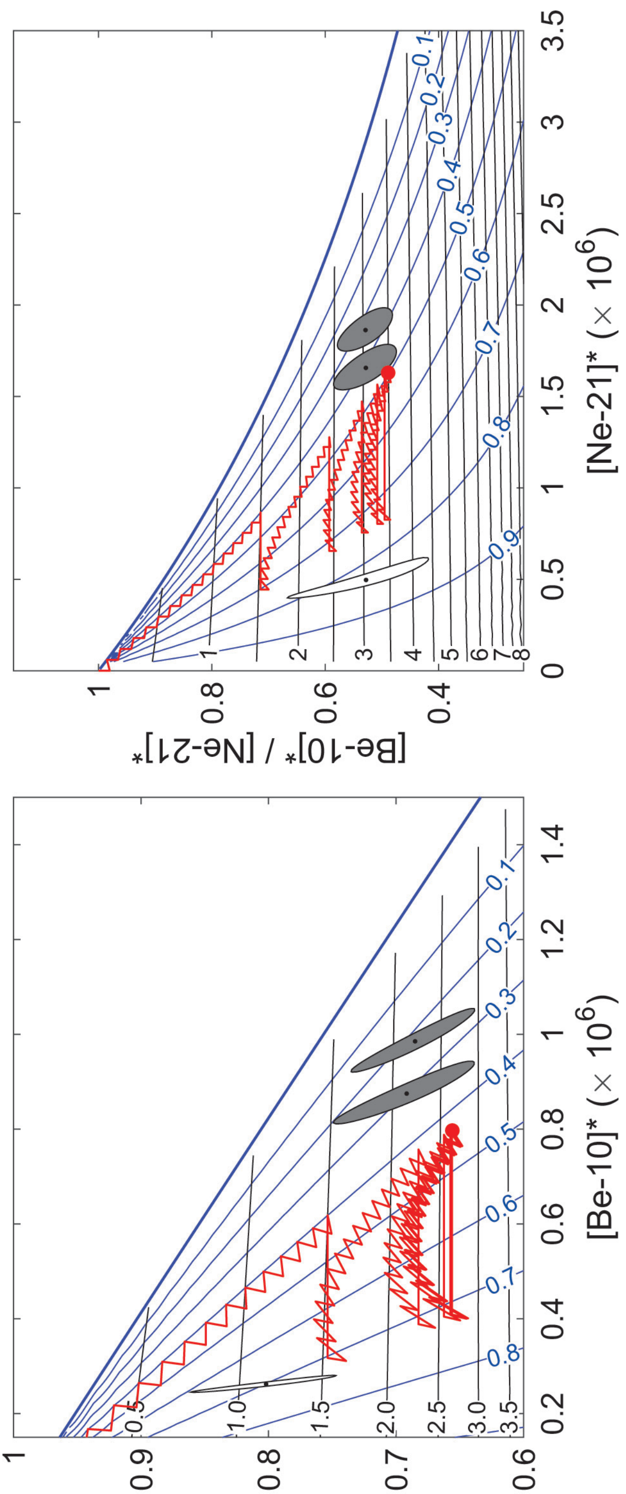

Fig. 16. ^{26}Al-^{10}Be (left) and ^{10}Be-^{21}Ne (right) diagrams showing the evolution of nuclide concentrations (red lines) for a hypothetical bedrock surface experiencing repeated 100 kyr glacial cycles over 9 Myr, during which the surface is ice-covered 40% of each cycle. Every 1.5 Myr, 100 cm of bedrock is removed by subglacial plucking. The red circle represents nuclide concentrations at the end of the scenario. Nuclide concentrations for samples from the Nash Hills are shown for comparison. The contours in figure 14 have limited meaning for samples that have experienced significant ice cover and/or non-steady erosion (for example, subglacial plucking). Here, the area below the simple-exposure line is contoured with blue isolines representing an upper limit on the fraction of each glacial cycle that a sample is ice-covered and black isolines representing a lower limit on the total time recorded by each sample (units: Myr).

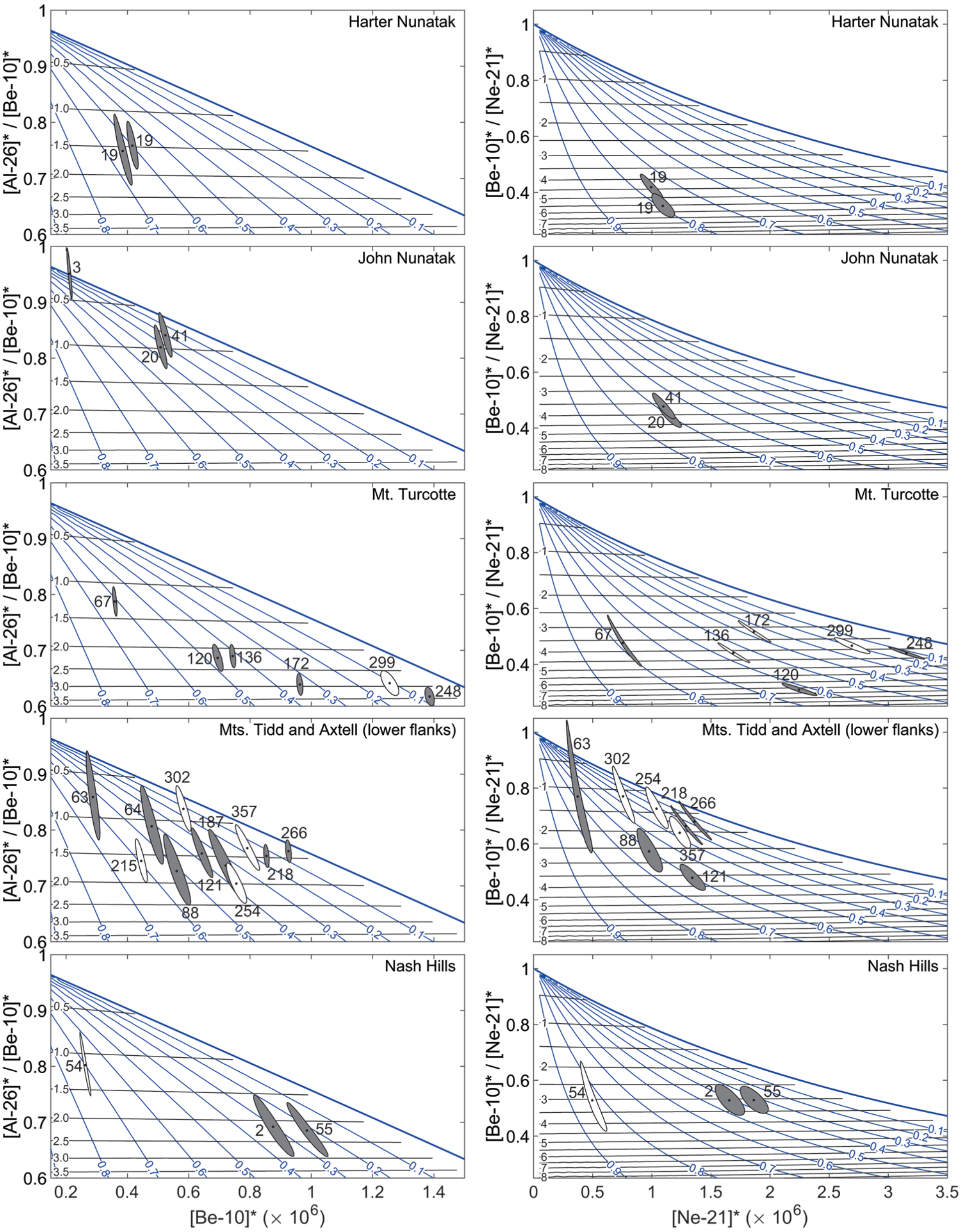

Fig. 17. ^{26}Al-^{10}Be (left) and ^{10}Be-^{21}Ne (right) diagrams for bedrock samples from sites in the Pirrit Hills and Nash Hills that have been ice-covered in the past. Refer to figure 16 for information about the contour lines.

constant with elevation. Therefore, a sample that deviates from these trends—that is, it has an apparent exposure age younger than a lower-elevation sample—must be eroded. We implement this identification procedure for ^{26}Al, ^{10}Be, and ^{21}Ne independently because each nuclide is sensitive to erosion on different timescales. Eroded samples are represented by white symbols in figures 14–18. Where a sample is

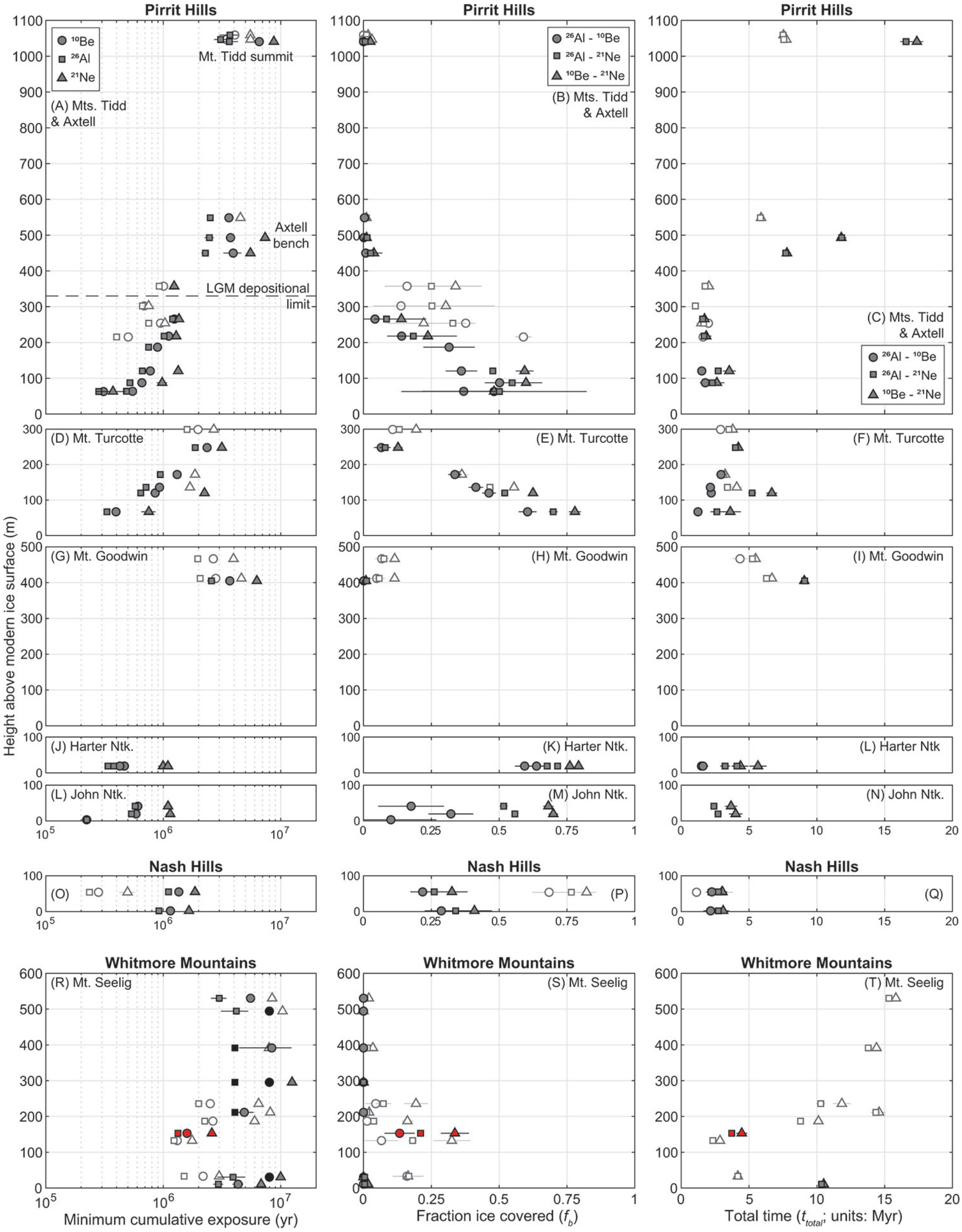

Fig. 18. Minimum cumulative exposure age (left column), fraction of each glacial cycle that each sample is covered by ice (middle column), and total time recorded by each sample (right column) for samples from the Pirrit Hills (upper 5 rows), Nash Hills, and Whitmore Mountains. Fraction covered and total time are calculated by solving equations 4–6. White symbols represent samples identified as eroded (see main text). Black symbols represent samples that are saturated with respect to a given nuclide. At saturation, nuclide concentrations are no longer time dependent and only provide lower limits on total exposure. For this figure, we assign saturated samples exposure ages equal to 4/λ, where λ is the ^{26}Al or ^{10}Be decay constant, which represents 98% of the time required to reach saturation or 4.1 and 8.0 Myr for ^{26}Al and ^{10}Be, respectively. Red symbols represent the Whitmore till. Error bars represent 68% confidence intervals. For many samples from the Whitmore Mountains and from above the trimline at the Pirrit Hills, the calculation of t_{total} does not produce meaningful values because of the assumed subaerial erosion rate of 5 cm Myr^{-1} (compare to fig. 15), and these samples are not shown in this figure.

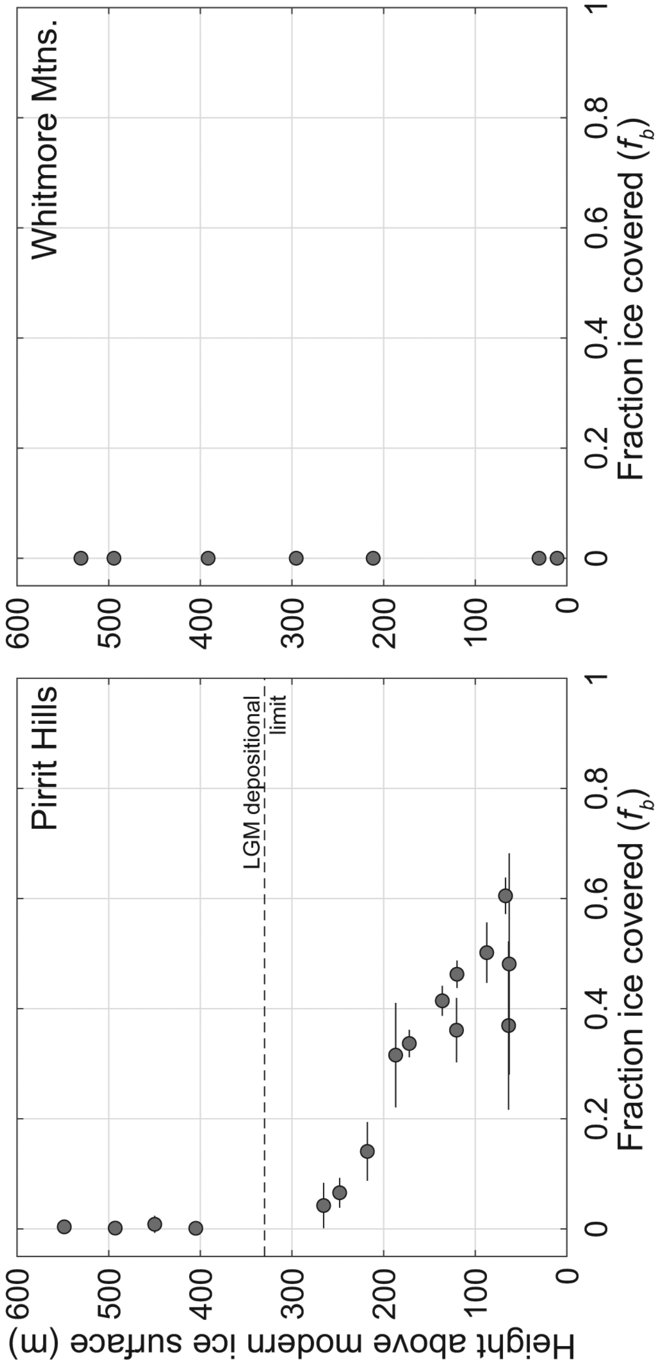

Fig. 19. Fraction of each glacial cycle that bedrock samples from the Pirrit Hills massif (Mts. Axtell, Tidd, Goodwin, and Turcotte) and the Whitmore Mtns. are ice-covered. Results are shown for the ^{26}Al-^{10}Be nuclide pair, which provide the best estimate of the true ice-cover fraction. Samples identified as eroded (see main text) have been removed.

represented by two nuclides (for example, a ^{26}Al/^{10}Be ratio), it is considered to be eroded if either or both nuclides indicate erosion.

This procedure reduces the noise in the dataset caused by erosion, and it also discards samples whose nuclide concentrations reflect only brief history. It cannot, however, identify all eroded samples. For example, sample 13-NTK-003-JHN was collected from John Nunatak from one of the only rounded landforms observed in the Pirrit Hills (fig. 7A), and it has significantly lower ^{26}Al and ^{10}Be exposure ages (^{21}Ne was not measured) than other samples from the same site (fig. 18). Despite the geomorphic evidence for glacial erosion, this sample is not labeled as eroded because it is the lowest-elevation sample from John Nunatak.

Constraints on Exposure Age and Subaerial Erosion Rates

Bedrock samples from the Whitmore Mountains and from above the trimline at the Pirrit Hills show no geomorphic evidence for past ice cover and have extremely old apparent exposure ages of 2 to 12 Myr (fig. 18). Four samples from the Whitmore Mountains are saturated with respect to ^{26}Al and/or ^{10}Be, which requires exposure for at least ~4.1 and ~8.0 Myr, respectively. Although, as described above, our production-rate calibration procedure assumes that these samples are saturated, this assumption is consistent with their ^{21}Ne exposure ages, and calibrating production rates in any other way would make these samples appear over-saturated with respect to ^{26}Al and ^{10}Be. Samples from the Whitmore Mountains and from above the Pirrit Hills trimline show large differences in ^{26}Al, ^{10}Be, and ^{21}Ne apparent exposure ages, which suggests that ^{26}Al and ^{10}Be concentrations have reached production-decay-erosion equilibrium, but ^{21}Ne concentrations have not. This is evident in two-nuclide diagrams where ^{26}Al-^{10}Be concentrations lie on the steady-erosion line but ^{10}Be-^{21}Ne concentrations plot in the simple-exposure region (fig. 14). Here we assume that these samples have experienced a single period of uninterrupted exposure at a steady erosion rate. We estimate both the exposure age t (years) and the erosion rate ε (cm Myr^{-1}) by solving the overdetermined system of equations:

$$N_{26} = \frac{P_{26}}{\lambda_{26} + \frac{\varepsilon}{\Lambda}}\left(1 - exp\left[-\left(\lambda_{26} + \frac{\varepsilon}{\Lambda}\right)t\right]\right) \tag{1}$$

$$N_{10} = \frac{P_{10}}{\lambda_{10} + \frac{\varepsilon}{\Lambda}}\left(1 - exp\left[-\left(\lambda_{10} + \frac{\varepsilon}{\Lambda}\right)t\right]\right) \tag{2}$$

$$N_{21} = \frac{P_{21}\Lambda}{\varepsilon}\left(1 - exp\left[\frac{-\varepsilon t}{\Lambda}\right]\right) \tag{3}$$

where N_i is the nuclide concentration (atoms g^{-1}), P_i is the production rate, and λ_i is the decay constant of nuclide i (Balco and others, 2014). The attenuation length for spallation (Λ) is taken to be 150 g cm^{-2}. The results indicate that the oldest bedrock samples from the Pirrit Hills and Whitmore Mountains have been exposed for around 9 to 12 Myr at erosion rates of 0 to 5 cm Myr^{-1} (fig. 15). This calculation does not produce meaningful ages for certain samples that overlap or lie below the steady-erosion line (fig. 14), and hence ages for these samples are not shown in figure 15. The contours in figure 14 show exposure ages and erosion rates calculated by solving equations 1–3 for the ^{26}Al-^{10}Be and ^{10}Be-^{21}Ne nuclide pairs.

As discussed below, the Whitmore till was likely deposited long ago by a wet-based mountain glacier and thus does not provide information about more recent variations in WAIS thickness. Although the till has an apparent ^{21}Ne exposure age of ~2.6 Myr, it appears to be a vestige of a larger deposit that has been mostly eroded away, suggesting that the true depositional age is much older. Concentrations of ^{26}Al, ^{10}Be and ^{21}Ne in the till are consistent with production-decay-erosion equilibrium (fig. 14), which precludes computing a finite exposure age using equations 1-3, but shows that the till was deposited more than ~7 Myr ago.

Constraints on Past Ice Cover

Geomorphic observations from below the trimline at the Pirrit Hills and from the Nash Hills indicate repeated, frozen-based ice cover and isolated instances of glacial erosion. Based on these observations, we hypothesize that nuclide concentrations in bedrock surfaces can be explained by a simple model in which surfaces are periodically covered by frozen-based ice for some fraction of glacial cycles. While this ice cover typically preserves subglacial surfaces, plucking occurs occasionally (Cuffey and others, 2000), which resets or significantly lowers nuclide concentrations. Figure 16 shows an example of how nuclide concentrations in a bedrock surface evolve according to this model and the assumptions that (i) glacial cycles have a constant duration (t_c, assumed to be 100 kyr) and (ii) that the fraction of each cycle that a sample is covered (f_b) is constant for each sample. Periodic exposure and ice cover cause nuclide concentrations to zig-zag down and to the right in two-nuclide space. Plucking, which decreases nuclide concentrations but does not affect nuclide ratios, moves the sample to the left. Nuclide concentrations recover with the resumption of periodic exposure and ice cover. This causes the sample to move to the right and eventually regain its original trajectory. Eventually, nuclide concentrations reach a dynamic equilibrium, whereby the pluck-recovery cycle causes them to "loop" in two-nuclide space (fig. 16).

This simple model captures many aspects of the glacial history that we infer from geomorphic observations, and, as shown by figure 16, it also provides an explanation for the general pattern that, in two-nuclide space, samples identified as eroded plot to the left of where we would expect them to be based on their elevation. Because the model, as described above, contains more parameters than we can invert for with three-nuclide data, we simplify it by assuming that each sample was initially plucked to sufficient depth to fully reset nuclide concentrations at some point in the past, and that no subglacial erosion has occurred since that time. At the end of *k* burial-exposure cycles, nuclide concentrations are given by:

$$N_{26}(k) = N_{26}(k-1)\,exp[-\lambda_{26} t_c f_b]\,exp\left[-\left(\lambda_{26}+\frac{\varepsilon}{\Lambda}\right)t_c(1-f_b)\right] + \frac{P_{26}}{\lambda_{26}}\left(1-exp\left[-\left(\lambda_{26}+\frac{\varepsilon}{\Lambda}\right)\right]t_c(1-f_b)\right) \tag{4}$$

$$N_{10}(k) = N_{10}(k-1)\,exp\,[-\lambda_{10} t_c f_b]\,exp\left[-\left(\lambda_{10}+\frac{\varepsilon}{\Lambda}\right)t_c(1-f_b)\right] + \frac{P_{10}}{\lambda_{10}}\left(1-exp\left[-\left(\lambda_{10}+\frac{\varepsilon}{\Lambda}\right)\right]t_c(1-f_b)\right) \tag{5}$$

$$N_{21}(k) = N_{21}(k-1)\,exp\left[-t_c(1-f_b)\frac{\varepsilon}{\Lambda}\right] + \frac{P_{21}\Lambda}{\varepsilon}\left(1-exp\left[-t_c(1-f_b)\frac{\varepsilon}{\Lambda}\right]\right) \tag{6}$$

We assume a slow subaerial erosion rate during interglacial periods (ε) of 5 cm Myr^{-1}, which is the average rate indicated by samples from above the Pirrit Hills trimline (fig. 15). For each nuclide pair, we compute f_b and the total time recorded t_{total} =

kt_c. Because time is a discrete variable, we solve Equations 4-6 by linear interpolation of values computed over two-nuclide space. Figures 16 and 17 are contoured for f_b and t_{total}.

The hypothetical scenario in figure 16 provides some intuition for how well the model captures true glacial history. Apparent f_b values at the end of the scenario are 0.43 and 0.5 for ^{26}Al-^{10}Be and ^{10}Be-^{21}Ne data, respectively, which are close to but slightly higher than the true value of 0.4. Computed f_b is always greater than or equal to true f_b, and therefore represents an upper limit. The short-lived nuclide pair ^{26}Al-^{10}Be typically provides the best estimate of f_b because the nuclide concentrations rebound more rapidly than the longer-lived pairs following a plucking event. Apparent t_{total} values at the end of the scenario are 2.6 Myr and 3.5 Myr for ^{26}Al-^{10}Be and ^{10}Be-^{21}Ne, respectively—much lower than the true 9 Myr history. Computed t_{total} underestimates true t_{total} for all nuclide pairs if plucking has occurred, and therefore represents a lower limit. The long-lived ^{10}Be-^{21}Ne pair always records the greatest t_{total} and therefore provides the best estimate of the actual history length. If the bedrock surface had been sampled immediately following a plucking event, we would have greatly overestimated f_b, but our estimate of t_{total} would be almost the same. If the surface was sampled during the recovery phase, our estimate of f_b would be closer to the actual value, and our estimate of t_{total} may be either higher or lower depending on where the sample is in two-nuclide space (fig. 16). We would have correctly inferred both f_b and t_{total} if the surface was sampled after only 1.5 Myr, before any simulated plucking.

One of the main assumptions of the model is that glacial cycles have a constant duration of 100 kyr. This assumption turns out to be unimportant. A lower value of t_c (for example, 40 kyr) and a proportionally greater number of cycles will produce nearly identical results as those shown in figures 16 and 17.

The results of this model for each sample and for the ^{26}Al-^{10}Be and ^{10}Be-^{21}Ne nuclide pairs are shown in figures 17 and 18. Below the Pirrit Hills trimline, f_b values increase toward the modern ice surface, where some samples appear to be covered for more than half of each glacial cycle (figs. 18 and 19). In contrast, samples from above the trimline and from the Whitmore Mountains indicate zero ice cover. Although the geometric constraint that f_b must decrease with elevation is not imposed in the model, this is nonetheless what is predicted. Samples identified as eroded (white symbols in fig. 18) imply higher f_b than other samples (fig. 18), which, as discussed above, is expected for recently plucked bedrock surfaces.

Samples below the trimline have t_{total} values of 1 to 7 Myr, while those from the Whitmore Mountains and from above the trimline record histories of ~8 Myr or longer (fig. 18). Although equations 1–3 and 4–6 are equivalent when $f_b = 0$, some high elevation samples show large differences between exposure ages (eqs. 1–3; fig. 17) and t_{total} (eqs. 4–6; fig. 18). This is probably due to two factors. First, t_{total} is computed with an assumed subaerial erosion rate of 5 cm Myr^{-1}, which is not representative for all high elevation samples (fig. 15). Second, t_{total} and exposure ages are computed from two- and three-nuclide data, respectively, and hence the results are sensitive to different time scales in the past. Therefore, if subaerial erosion rates have, in fact, changed over time, these two methods may produce different results depending on which nuclide pair is used to calculate t_{total}. Given these considerations, exposure ages are probably more representative than t_{total} of the true history for high elevation samples that show no evidence for past ice cover. The shorter histories recorded by samples below the trimline imply that these surfaces experience occasional plucking, and that the pluck-recovery loop prevents the apparent total history from increasing beyond a few million years even though the surface has been repeatedly glaciated by frozen-based ice for more than that amount of time. Samples identified as eroded yield total time estimates that are similar to estimates from other samples (fig. 18), which is presumably due to the fact that plucking has a minor influence on t_{total} (fig. 16).

To summarize, we have shown that a simple model of periodic exposure and ice cover over glacial cycles that is motivated by geomorphic observations can explain observed nuclide concentrations in bedrock surfaces. Combined with geomorphic observations, the results indicate that while bedrock surfaces at the Whitmore Mountains and above the Pirrit Hills trimline have experienced millions of years of uninterrupted exposure at very low erosion rates, surfaces below the trimline have been repeatedly covered by frozen-based ice that occasionally and sporadically plucked subglacial bedrock surfaces. Samples that are identified as eroded because they do not follow monotonic age-elevation profiles can be explained as the result of recent plucking.

DISCUSSION

Ice Thickness Variations in West Antarctica

Over glacial cycles, the two processes that exert the greatest influence on the thickness of the WAIS are changes in the position of the margin and changes in the accumulation rate. Advance or retreat of the margin propagates a wave of dynamic thickening or thinning, respectively, that damps as it progresses upstream (Alley and Whillans, 1984). This results in maximum and earliest thickness change near the margin and minimal and most delayed change at the divide. Dynamic thickness change is opposed by changes in the accumulation rate, which increases during interglacial periods, in part because a warmer atmosphere can hold more moisture. In West Antarctica, the WAIS Divide ice core indicates that accumulation rates were much lower than present for tens of millennia during the last glacial period (Buizert and others, 2015) and roughly doubled 18 to 15 kyr ago (Fudge and others, 2016). East Antarctic ice cores show similar patterns and indicate that reduced accumulation rates are a consistent feature of Pleistocene glacial periods (Parrenin and others, 2007).

Spector and others (2019) report (i) ^{10}Be exposure ages on glacial deposits from the Pirrit Hills and (ii) cosmogenic ^{14}C measurements for many of the same bedrock samples from Mt. Seelig that we discuss here. At the Pirrit Hills, the WAIS reached a highstand ~330 m above present during the last ice age while accumulation rates in West Antarctica were at their ice-age low, and subsequent thinning coincided with retreat of the margin downstream in the Weddell Sea (Johnson and others, 2019). Other sites in the Weddell Sea sector appear to have similar glacial histories (Bentley and others, 2010, 2017; Hein and others, 2016; Balco and others, 2016; Nichols and others, 2019), implying that thickness changes at these sites are primarily controlled by the position of the margin downstream. At the Whitmore Mtns., Spector and others (2019) find that the WAIS was thicker than present for a period of less than ~ 8 kyr within the past 15 kyr, but was probably the same thickness or thinner than present during the last ice age when accumulation rates in West Antarctica were at a minimum (Fudge and others, 2016). These findings are consistent with the hypothesis that the divide initially thickened early in the deglaciation due to the deglacial rise in the accumulation rate and subsequently thinned in response to retreat of the ice-sheet margin (Steig and others, 2001).

The results of this paper indicate that much of the behavior described by Spector and others (2019) was not limited to the last ice age but has been a persistent pattern of WAIS thickness change over glacial cycles. Geomorphic observations and cosmogenic-nuclide measurements on bedrock surfaces show that the lower flanks of the Pirrit and Nash Hills have been repeatedly covered by a thicker WAIS, and at least some pre-LGM highstands were of similar magnitude to the LGM highstand of ~330 m. Although ^{14}C measurements on bedrock surfaces from the Whitmore Mountains indicate a brief period of ice cover during the last deglaciation, ^{26}Al, ^{10}Be, and ^{21}Ne results demonstrate that episodes of thicker-than-present ice at the Whitmore Mountains were very brief and rare, and that, on 10^5-10^6 year timescales, the divide has been no thicker than present the vast majority of the time (fig. 19).

Although it is conceivable that, with the exception of rare and transient episodes of thicker ice, the divide has remained at a constant thickness over many glacial cycles, this scenario is unlikely as accumulation rate changes would need to be perfectly balanced by dynamic ice-thickness changes related to the position of the margin. We hypothesize that the divide has typically been thinner than present. During the Pleistocene, this would likely have been due to reduced accumulation during glacial periods, which has been suggested for the last ice age in both East and West Antarctica on the basis of ice-core analyses (Steig and others, 2001; Parrenin and others, 2007) and has been simulated by ice-sheet models (Pollard and others, 2016; Spector and others, 2018). Ice-sheet collapse events would also be expected to draw down ice in central West Antarctica (Spector and others, 2018). Such events, if they occurred, likely only represented a small fraction of the Pleistocene, but may have been more prolonged during warmer climates of the late Miocene and Pliocene.

At the Pirrit Hills, evidence for thinner ice is in the form of weathered bedrock surfaces that intersect and appear to descend beneath the modern ice surface. Although this implies lower ice levels in the past (Mercer, 1968; Mukhopadhyay and others, 2012), it does not indicate the timing nor the magnitude of past thinning. Because the WAIS at the Pirrit Hills was thicker than present during recent glacial periods, any thinning below the modern level presumably must have occurred during Pleistocene interglacial periods and/or earlier times during the late Miocene or Pliocene. Although a thinner WAIS at the Pirrit Hills is consistent with the hypothesis of past ice sheet collapse, it is equally consistent with less extreme scenarios, such as slightly lower accumulation rates during past interglacial periods.

Mid-Miocene Formation of Alpine Glacial Landscapes

The wet-based glaciers that carved the alpine landscapes of West Antarctic nunataks disappeared prior to the development of the weathered bedrock surfaces that superimpose these landscapes. The oldest exposure ages from the Whitmore Mountains and Pirrit Hills demonstrate that this occurred at least ~12 Myr ago, and that, since that time, surface erosion rates have remained extraordinarily low. Such low erosion rates result from the polar desert climate and the complete lack of liquid water and biota in high elevation regions of Antarctica. Marine sedimentary records indicate that this climate was established 14 to 15 Myr ago during the abrupt mid-Miocene cooling (Zachos and others, 2001; Shevenell and others, 2004), and in Antarctica, this hypothesis is supported by several lines of evidence (see review by Sugden and others, 2017), summarized below.

Fossil organisms and pollen in terrestrial and marine sediments from sites spanning the continent show that a tundra environment existed during the mid-Miocene and appears to have gone extinct ~14 Myr ago, replaced by polar conditions that have persisted to the present (Ashworth and Cantrill, 2004; Lewis and others, 2008; Warny and others, 2009; Anderson and others, 2011; Wei and others, 2014; Ashworth and Erwin, 2016). In southern Victoria Land, recovered taxa suggest mean summer temperatures up to ~5 to 10 °C prior to the cooling (Lewis and others, 2008; Warny and others, 2009), and there is an array of well preserved subglacial erosional features, such as scabland and pothole systems, that formed ~14 Myr ago (Denton and

Sugden, 2005). A switch from wet- to frozen-based glaciation in the Olympus Range has also been dated to ~14 Myr B.P. and implies a cooling of ~8 °C (Lewis and others, 2007, 2008), similar to the 6 to 7 °C cooling estimated for surface waters in the southwest Pacific (Shevenell and others, 2004). In inland Marie Byrd Land, volcanoes with well developed cirques are only found on pre-mid-Miocene edifices (Rocchi and others, 2006), suggesting a switch to frozen-based glaciation at this time.

Based on (i) this evidence for the establishment of the polar desert climate 14 to 15 Myr ago and (ii) exposure ages that demonstrate bedrock surface preservation for at least 12 Myr, we hypothesize that alpine landscapes in West Antarctica were carved by mountain glaciers during the relatively warm climates of the mid-Miocene (and possibly also during the early Miocene), and that they have been preserved as vestiges of that time since the subsequent cooling 14 to 15 Myr ago. Support for this hypothesis comes from ice-sheet model simulations forced by warm mid-Miocene boundary conditions that depict a largely deglaciated West Antarctica with wet-based glaciers and small ice caps persisting in mountain regions (Jamieson and others, 2010; Gasson and others, 2016). Marine sedimentary records indicate that such climates existed for at least a few million years prior to the mid-Miocene cooling (for example Zachos and others, 2001), which would be sufficient for the development of alpine landscapes. This hypothesis predicts that no rock surface in West Antarctica is older than 14 to 15 Myr, and a recent compilation of exposure-age data shows that this is, in fact, the case for surfaces across Antarctica (Spector and Balco, 2020). The simplest explanation for the Whitmore till, which as described above, is characteristic of wet-based glacial deposits, is that it was deposited during or shortly before the mid-Miocene cooling.

Extension of the Ellsworth Trimline in the Pirrit Hills

The trimline in the Pirrit Hills occurs across the massif at an elevation of around 1600 to 1700 m and marks a transition between blunt-crested ridges below and serrated ridge crests above. Above the trimline all bedrock surfaces show advanced stages of subaerial weathering and there is zero indication of past ice cover, while below, bedrock surfaces are generally less weathered, and there is isolated evidence for glacial erosion. The trimline coincides with or is similar to the height of the LGM depositional limit, below which glacial debris has exposure ages ranging from Holocene to at least ~1 Myr (Spector and others, 2019), indicating deposition over multiple ice ages.

Denton and others (1992) describe a very similar trimline in the Ellsworth Mountains to the north of the Pirrit Hills, and we summarize their descriptions here. The Ellsworth trimline is etched across ridges and spurs of the relic alpine landscape of the Ellsworth Mountains and delineates highly serrated ridge crests above from smoothed crests below. The serrations commonly form closely spaced, delicate spires that are up to 30 m in height. Below the trimline, the alpine topography is well preserved, but ridge crests are blunted. Striations are common below the trimline, and, in places, particularly at lower elevation, bedrock surfaces are mantled with glacial debris. Evidence for past ice cover is completely absent above the trimline.

The trimline is most conspicuous in the Sentinel Range, which comprises the northern and higher elevation portion of the Ellsworth Mountains. Most of the Heritage Range to the south lies below the trimline, which occurs there discontinuously on high peaks and ridges. Trimline elevations vary smoothly over the length of the Sentinel Range in a pattern consistent with the surface of an ice sheet or ice cap (fig. 20). The trimline is highest on the west side of the Sentinel Range; it is found at lower elevations both on the east side of the Sentinel Range (not shown in fig. 20)

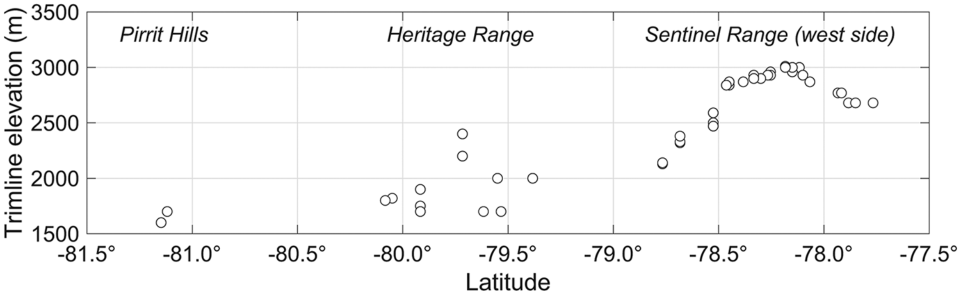

Fig. 20. Trimline elevations in the Ellsworth Mountains (Denton and others, 1992) and Pirrit Hills as a function of latitude. Denton and others (1992) report that on the east side of the Sentinel Range (not shown in figure), trimline elevations are 2440–2680 m near the range divide, and further east, adjacent to Rutford Ice Stream range, from 1950 in the south to 2470 m in the north.

and in the Heritage Range. The trimline in the Pirrit Hills is slightly lower than the trimline in the Heritage Range.

The very similar geomorphic characteristics and the consistent elevation pattern of the Pirrit Hills and Ellsworth trimlines suggest that they are part of the same feature. The primary differences are that (i) ridge crest serrations in the Pirrit Hills are more subtle than those in the Ellsworth Mountains, and (ii) evidence for wet-based glacial erosion below the trimline is absent in the Pirrit Hills. These differences can be explained by differences in lithology. In the Ellsworth Mountains, the trimline is primarily cut into the resistant Crashsite Group quartzite, which holds striations well and does not easily weather by granular disintegration or exfoliation (Denton and others, 1992). In contrast, the Pirrit Hills granite weathers primarily by granular disintegration and exfoliation, and we do not expect it to hold striations as well as Crashsite quartzite. Notably, striations have been observed in (i) sedimentary rocks near the modern ice level at Moreland Nunatak, a minor peak ~20 km west of the Pirrit Hills and (ii) a few hundred meters above the modern ice level in the Martin Hills, 110 km southwest of the Pirrit Hills (The Polar Rock Repository, 2009). Therefore, to summarize, because differences between the Pirrit Hills and Ellsworth trimlines can be easily accounted for, we conclude that they are, in fact, the same feature.

Denton and others (1992) argue that the trimline formed at or a short distance below a former ice surface on the basis of (i) the smoothly-varying elevation of the trimline; (ii) the complete absence of evidence for ice cover above it; (iii) the orientation of striations below the trimline, which are perpendicular to the implied former ice surface; and (iv) the scarcity of glacial debris near the trimline, which is consistent with the idea that it formed in an accumulation zone where flowlines are oriented downward. This scenario implies that the trimline was etched by thin, yet wet-based ice cover sometime after the development of the alpine glacier landscape, which, as discussed above, appears to have formed during or prior to the mid-Miocene climate transition 14 to 15 Myr ago. Sugden and others (2017) suggest that the main phase of trimline erosion occurred during or shortly after the mid-Miocene cooling and the transition from alpine to continental glaciation.

Sugden and others (2017) also report exposure-age data from the Heritage Range that place a minimum age of ~3.5 Myr on the development of eroded surfaces below the trimline. This age is the sum of apparent exposure and burial ages assuming a two-stage exposure-burial history. Using this method, bedrock samples from below the trimline at the Pirrit Hills record similar minimum exposure-burial histories of up to ~3.6 Myr. Although this may appear to suggest that the trimline formed long after the mid-Miocene, the model we described above demonstrates how apparent histories of a few million years can be consistent with much longer histories of exposure, frozen-based ice cover, and occasional subglacial plucking. Stronger constraints on the age of the trimline could likely be derived from exposure dating of the striated bedrock surfaces located just below the trimline in the Sentinel Range.

CONCLUSIONS

At the Whitmore Mountains and above the trimline in the Pirrit Hills there is no evidence for past ice cover, and cosmogenic nuclide concentrations in the oldest bedrock surfaces indicate continuous exposure for ~12 Myr at extremely low erosion rates. This establishes that alpine landforms at these sites were carved by mountain glaciers prior to this time, and we hypothesize that this occurred during the relatively warm climates prior to the mid-Miocene climate transition 14 to 15 Myr ago. Below the trimline, bedrock surfaces have nuclide concentrations that are most easily explained by repeated frozen-based ice cover and occasional subglacial plucking, which is consistent with geomorphic observations. Surfaces near the modern ice level appear to have been covered for more than half of the time, while higher elevation surfaces indicate progressively less ice cover.

At all of our field sites, weathered bedrock surfaces with very high cosmogenic-nuclide concentrations intersect the modern ice level, implying lower ice levels in the past. At the Pirrit Hills and Nash Hills, the WAIS was thicker than present during glacial periods, and so any thinning presumably occurred during past interglacial periods. In contrast, at the Whitmore Mountains the WAIS has almost never been thicker than present, and we hypothesize that the divide here was typically thinner than present during Pleistocene glacial periods when accumulation rates were very low.

Based on the similarity of the Pirrit Hills and Ellsworth trimlines and their associated geomorphic features, we conclude that they are, in fact, part of the same feature. Although bedrock surfaces below the trimline have apparent exposure histories up to ~3.5 Myr, the trimline is hypothesized to have formed 14-15 Myr ago during warmer-than-present climates of the mid-Miocene (Sugden and others, 2017). We demonstrate that this apparent contradiction can be explained by the scenario of repeated frozen-based ice cover and occasional subglacial plucking described above.

ACKNOWLEDGMENTS

Support for this work was provided by US National Science Foundation (NSF) grants OPP-1142162 and OPP-1341728, and the Ann and Gordon Getty Foundation. Spector received funding from the NSF Graduate Research Fellowship Program. We thank Maurice Conway and Tom Schaefer for assistance with field work. Danielle Lemmon and Jessica Badgeley assisted with lab work. Robert Finkel, Susan Zimmerman, and Tom Brown assisted with AMS measurements. Geospatial support for this work was provided by the Polar Geospatial Center under NSF OPP awards 1043681 and 1559691. We thank Robert Ackert and David Sugden for helpful and comprehensive reviews.

APPENDIX

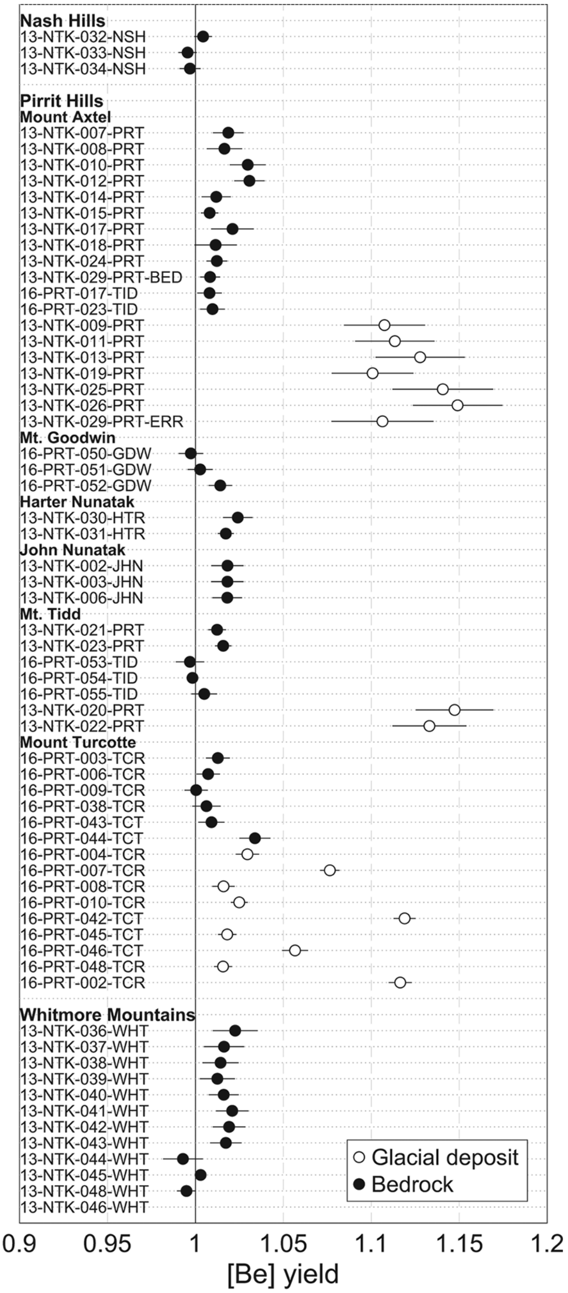

Fig. A1. Beryllium yield for bedrock samples reported in this paper and for glacial deposits described by Spector and others (2019). Beryllium yield is the quotient of the Be mass measured by ICPOES and the Be mass added as carrier. Error bars represent 68% confidence intervals.

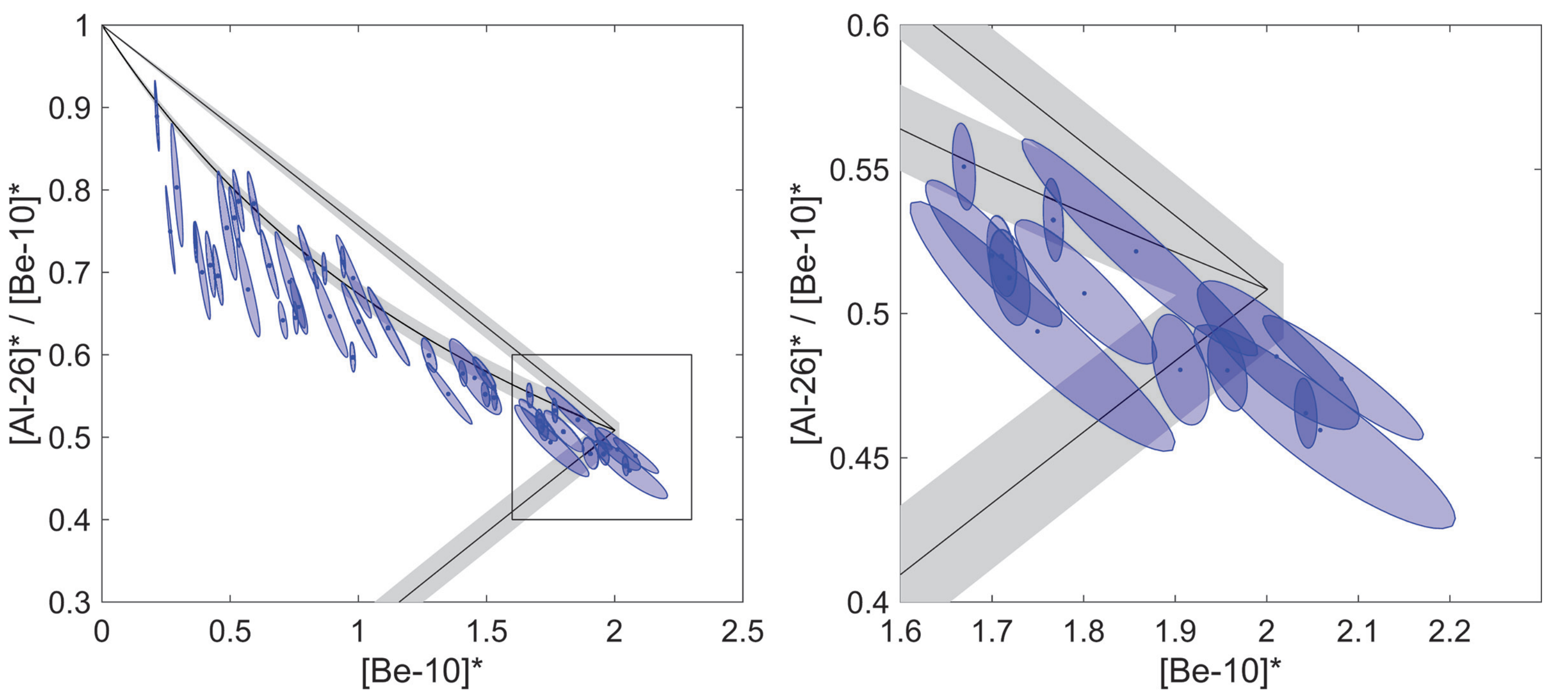

Fig. A2. Left panel: ^{26}Al-^{10}Be diagram for all of the samples reported in this paper on which ^{26}Al and ^{10}Be concentrations have been measured. The upper black line is the 'simple exposure line', which represents nuclide concentrations resulting from continuous exposure and zero erosion. The middle black line is the 'steady erosion line', which represents steady surface erosion for long enough that nuclide concentrations have reached equilibrium. The lower black line represents nuclide concentrations under the hypothetical two-stage scenario of (i) exposure with zero erosion for sufficiently long that ^{26}Al and ^{10}Be concentrations have reached equilibrium (which requires >8 Myr for ^{10}Be), and (ii) subsequent burial during which nuclide production is completely stopped. The gray bands around the black lines represent the effect of accounting for uncertainty in the half-lives of ^{26}Al and ^{10}Be. Ellipses represent 68% confidence regions representing measurement uncertainty and production-rate uncertainty. Nuclide concentrations are normalized to local production rates ($N^* = N/P$, where N is the nuclide concentration and P is the local production rate). However, in contrast to figure 14, which uses locally calibrated production rates, here we show the effect of basing production rates on the commonly used calibration datasets of Borchers and others (2016). Of note is that some of the samples with very high ^{26}Al and ^{10}Be concentrations, which are mostly from the Whitmore Mountains, plot to the right of the black lines and gray bands, which is not physically possible if production rates have been accurately estimated. The right panel enlarges the area within the black box in the left panel.

REFERENCES

Alley, R. B., and Whillans, I. M., 1984, Response of the East Antarctica ice sheet to sea-level rise: Journal of Geophysical Research, p. 6487, https://doi.org/10.1029/JC089iC04p06487

Anderson, J. B., Warny, S., Askin, R. A., Wellner, J. S., Bohaty, S. M., Kirshner, A. E., Livsey, D. N., Simms, A. R., Smith, T. R., Ehrmann, W., Lawver, L. A., Barbeau, D., Wise, S. W., Kulhanek, D. K., Weaver, F. M., and Majewski, W., 2011, Progressive Cenozoic cooling and the demise of Antarctica's last refugium: Proceedings of the National Academy of Sciences of the United States of America, p. 11356–11360, https://doi.org/21709269

Ashworth, A. C., and Cantrill, D. J., 2004, Neogene vegetation of the Meyer Desert Formation (Sirius Group) Transantarctic Mountains, Antarctica: Palaeogeography, Palaeoclimatology, Palaeoecology, v. 213, n. 1–2, p. 65–82, https://doi.org/10.1016/S0031-0182(04)00359-1

Ashworth, A. C., and Erwin, T. L., 2016, *Antarctotrechus balli* sp. n. (Carabidae, Trechini): The first ground beetle from Antarctica: ZooKeys, v. 635, p. 109–122, https://doi.org/10.3897/zookeys.635.10535

Balco, G., 2017, Production rate calculations for cosmic-ray-muon-produced ^{10}Be and ^{26}Al benchmarked against geological calibration data: Quaternary Geochronology, v. 39, p. 150–173, https://doi.org/10.1016/j.quageo.2017.02.001

Balco, G., and Shuster, D. L., 2009, Production rate of cosmogenic ^{21}Ne in quartz estimated from ^{10}Be, ^{26}Al, and ^{21}Ne concentrations in slowly eroding Antarctic bedrock surfaces: Earth and Planetary Science Letters, v. 281, n. 1–2, p. 48–58, https://doi.org/10.1016/j.epsl.2009.02.006

Balco, G., Stone, J. O. H., Sliwinski, M. G., and Todd, C., 2014, Features of the glacial history of the Transantarctic Mountains inferred from cosmogenic ^{26} Al, ^{10} Be and ^{21} Ne concentrations in bedrock surfaces: Antarctic Science, v. 26, n. 6, p. 708–723, https://doi.org/10.1017/S0954102014000261

Balco, G., Todd, C., Huybers, K., Campbell, S., Vermeulen, M., Hegland, M., Goehring, B. M., and Hillebrand, T. R., 2016, Cosmogenic-nuclide exposure ages from the Pensacola Mountains adjacent to the Foundation Ice Stream, Antarctica: American Journal of Science, v. 316, n. 6, p. 542–577, https://doi.org/10.2475/06.2016.02

Balco, G., Blard, P.-H., Shuster, D. L., Stone, J. O. H., and Zimmermann, L., 2019, Cosmogenic and nucleogenic ^{21}Ne in quartz in a 28-meter sandstone core from the McMurdo Dry Valleys, Antarctica: Quaternary Geochronology, v. 52, p. 63–76, https://doi.org/10.1016/j.quageo.2019.02.006

Bentley, M. J., Fogwill, C. J., Kubik, P. W., and Sugden, D. E., 2006, Geomorphological evidence and cosmogenic ^{10}Be/^{26}Al exposure ages for the Last Glacial Maximum and deglaciation of the Antarctic Peninsula Ice Sheet: GSA Bulletin, v. 118, n. 9–10, p. 1149–1159, https://doi.org/10.1130/B25735.1

Bentley, M. J., Fogwill, C. J., Le Brocq, A. M., Hubbard, A. L., Sugden, D. E., Dunai, T. J., and Freeman, S. P. H. T., 2010, Deglacial history of the West Antarctic Ice Sheet in the Weddell Sea embayment: Constraints on past ice volume change: Geology, v. 38, n. 5, p. 411–414, https://doi.org/10.1130/G30754.1

Bentley, M. J., Hein, A. S., Sugden, D. E., Whitehouse, P. L., Shanks, R., Xu, S., and Freeman, S. P. H. T., 2017, Deglacial history of the Pensacola Mountains: Quaternary Science Reviews, v. 158, p. 58–76, https://doi.org/10.1016/j.quascirev.2016.09.028

Borchers, B., Marrero, S., Balco, G., Caffee, M., Goehring, B., Lifton, N., Nishiizumi, K., Phillips, F., Schaefer, J., and Stone, J., 2016, Geological calibration of spallation production rates in the CRONUS-Earth project: Quaternary Geochronology, v. 31, p. 188–198, https://doi.org/10.1016/j.quageo.2015.01.009

Bruno, L. A., Baur, H., Graf, T., Schlüchter, C., Signer, P., and Wieler, R., 1997, Dating of Sirius Group tillites in the Antarctic Dry Valleys with cosmogenic ^{3}He and ^{21}Ne: Earth and Planetary Science Letters, v. 147, p. 37–54, https://doi.org/10.1016/S0012-821X(97)00003-4

Buizert, C., Cuffey, K. M., Severinghaus, J. P., Baggenstos, D., Fudge, T. J., Steig, E. J., Markle, B. R., Winstrup, M., Rhodes, R. H., Brook, E. J., Sowers, T. A., Clow, G. D., Cheng, H., Edwards, R. L., Sigl, M., McConnell, J. R., and Taylor, K. C., 2015, The WAIS Divide deep ice core WD2014 chronology–Part 1: Methane synchronization (68–31 kaBP) and the gas age–ice age difference: Climate of the Past, v. 11 n. 2, p. 153–173, https://doi.org/10.5194/cp-11-153-2015

Craddock, J. P., Schmitz, M. D., Crowley, J. L., Larocque, J., Pankhurst, R. J., Juda, N., Konstantinou, A., and Storey, B., 2017, Precise U-Pb zircon ages and geochemistry of Jurassic granites, Ellsworth-Whitmore terrane, central Antarctica: GSA, Bulletin, v. 129, n. 1 – 2, p. 118–136, https://doi.org/10.1130/B31485.1

Cuffey, K. M., Conway, H., Gades, A. M., Hallet, B., Lorrain, R., Severinghaus, J. P., Steig, E. J., Vaughn, B., and White, J. W. C., 2000, Entrainment at cold glacier beds: Geology, v. 28, n. 4, p. 351–354, https://doi.org/10.1130/0091-7613(2000)28<351:EACGB>2.0.CO;2

Denton, G. H., and Sugden, D. E., 2005, Meltwater features that suggest Miocene ice-sheet overriding of the transantarctic mountains in Victoria Land, Antarctica: Geografiska Annaler: Series A, Physical Geography, v. 87, n. 1, p. 67–85, https://doi.org/10.1111/j.0435-3676.2005.00245.x

Denton, G. H., Bockheim, J. G., Wilson, S. C., and Schlüchter, C., 1986, Late Cenozoic History of Rennick Glacier and Talos Dome, Northern Victoria Land, Antarctica: Geological Investigations in Northen Victoria Land: Antarctic Research Series, v. 46, p. 339–375, https://doi.org/10.1002/9781118664957.ch16

Denton, G. H., Bockheim, J. G., Rutford, R. H., and Andersen, B. G., 1992, Chapter 22, Glacial history of the Ellsworth Mountains, West Antarctica: GSA Memoirs, v. 170, p. 403–432.

Ditchburn, R. G., and Whitehead, N. E.,1994, The separation of ^{10}Be from silicates: Canberra, Australia, Proceedings of the 3rd Workshop of the South Pacific Environmental Radioactivity Association.

Fernandez-Mosquera, D., Hahm, D., and Marti, K., 2010, Calculated rates of cosmic ray muon-produced Ne in subsurface quartz: Geophysical Research Letters, v. 37, n. 15, https://doi.org/10.1029/2010GL044106

Fitzgerald, P. G., and Stump, E., 1991, Early Cretaceous Uplift in the Ellsworth Mountains of West Antarctica: Science, v. 254, n. 5028, p. 92–94, https://doi.org/17739957

Fretwell, P., Pritchard, H. D., Vaughan, D. G., Bamber, J. L., Barrand, N. E., Bell, R., Bianchi, C., Bingham, R. G., Blankenship, D. D., Casassa, G., Catania, G., Callens, D., Conway, H., Cook, A. J., Corr, H. F. J. D., Damaske, D., Damm, V., Ferraccioli, F., Forsberg, R., Fujita, S., Gim, Y., Gogineni, P., Griggs, J. A., Hindmarsh, R. C. A., Holmlund, P., Holt, J. W., Jacobel, R. W. A., Jenkins, A., Jokat, W., Jordan, T., King, E. C., Kohler, J., Krabill, W., Riger-Kusk, M., Langley, K. A., Leitchenkov, G., Leuschen, C., Luyendyk, B. P., Matsuoka, K., Mouginot, J., Nitsche, F. O., Nogi, F., Nost, O. A., Popov, S. V., Rignot, E., Rippin, D. M., Rivera, A., Roberts, J., Ross, N., Siegert, M. J., Smith, A. M., Steinhage, D., Studinger, M., Sun, B., Tinto, B. K., Welch, B. C., Wilson, D., Young, D. A., Xiangbin, C., and Zirizzotti, A., 2013, Bedmap2: Improved ice bed, surface and thickness datasets for Antarctica: The Cryosphere, v. 7, p. 375–393, https://doi.org/10.5194/tc-7-375-2013

Fudge, T. J., Markle, B. R., Cuffey, K. M., Buizert, C., Taylor, K. C., Steig, E. J., Waddington, E. D., Conway, H., and Koutnik, M., 2016, Variable relationship between accumulation and temperature in West Antarctica for the past 31,000 years: Geophysical Research Letters, v. 43, n. 8, p. 3795–3803, https://doi.org/10.1002/2016GL068356

Gasson, E., DeConto, R. M., Pollard, D., and Levy, R. H., 2016, Dynamic Antarctic ice sheet during the early to mid-Miocene: Proceedings of the National Academy of Sciences of the United States of America, v. 113, n. 13, p. 3459–3464, https://doi.org/26903645

Hein, A. S., Marrero, S. M., Woodward, J., Dunning, S. A., Winter, K., Westoby, M. J., Freeman, S. P. H. T., Shanks, R. P., and Sugden, D. E., 2016, Mid-Holocene pulse of thinning in the Weddell Sea sector of the West Antarctic ice sheet: Nature Communications, v. 7, p. 12511, https://doi.org/27545202

Hetzel, R., Niedermann, S., Ivy-Ochs, S., Kubik, P. W., Tao, M., and Gao, B., 2002, ^{21}Ne versus ^{10}Be and ^{26}Al exposure ages of fluvial terraces: The influence of crustal Ne in quartz: Earth and Planetary Science Letters, v. 201, n. 3–4, p. 575–591, https://doi.org/10.1016/S0012-821X(02)00748-3

Holmlund, P., and Näslund, J.-O., 1994, The glacially sculptured landscape in Dronning Maud Land, Antarctica, formed by wet-based mountain glaciation and not by the present ice sheet: Boreas, v. 23, n. 2, p. 139–148, https://doi.org/10.1111/j.1502-3885.1994.tb00594.x

Howat, I. M., Porter, C., Smith, B. E., Noh, M.-J., and Morin, P., 2019, The Reference Elevation Model of Antarctica: The Cryosphere, v. 13, n. 2, p. 665–674, https://doi.org/10.5194/tc-13-665-2019

Jamieson, S. S. R., Sugden, D. E., and Hulton, N. R. J., 2010, The evolution of the subglacial landscape of Antarctica: Earth and Planetary Science Letters, v. 293, n. 1–2, p. 1–27, https://doi.org/10.1016/j.epsl.2010.02.012

Johnson, J. S., Nichols, K. A., Goehring, B. M., Balco, G., and Schaefer, J. M., 2019, Abrupt mid-Holocene ice loss in the western Weddell Sea Embayment of Antarctica: Earth and Planetary Science Letters, v. 518, p. 127–135, https://doi.org/10.1016/j.epsl.2019.05.002

Lewis, A. R., Marchant, D. R., Ashworth, A. C., Hemming, S. R., and Machlus, M. L., 2007, Major Middle Miocene global climate change: Evidence from East Antarctica and the Transantarctic Mountains: GSA Bulletin, v. 119, n. 11–12, p. 1449–1461, https://doi.org/10.1130/0016-7606(2007)119[1449:MMMGCC]2.0.CO;2

Lewis, A. R., Marchant, D. R., Ashworth, A. C., Hedenas, L., Hemming, S. R., Johnson, J. V., Leng, M. J., Machlus, M. L., Newton, A. E., Raine, J. I., Willenbring, J. K., Williams, M., and Wolfe, A. P., 2008, Mid-Miocene cooling and the extinction of tundra in continental Antarctica: Proceedings of the National Academy of Sciences of the United States of America, v. 105, n. 31, p. 10676–10680, https://doi.org/18678903

Lifton, N., 2016, Implications of two Holocene time-dependent geomagnetic models for cosmogenic nuclide production rate scaling: Earth and Planetary Science Letters, v. 433, p. 257–268, https://doi.org/10.1016/j.epsl.2015.11.006

Lifton, N., Sato, T., and Dunai, T. J., 2014, Scaling *in situ* cosmogenic nuclide production rates using analytical approximations to atmospheric cosmic-ray fluxes: Earth and Planetary Science Letters, v. 386, p. 149–160, https://doi.org/10.1016/j.epsl.2013.10.052

Marchant, D. R., and Denton, G. H., 1996, Miocene and Pliocene paleoclimate of the Dry Valleys region, Southern Victoria land: A geomorphological approach: Marine Micropaleontology, v. 27, n. 1–4, p. 253–271, https://doi.org/10.1016/0377-8398(95)00065-8

Mercer, J. H., 1963, Glacial Geology of Ohio Range, Central Horlick Mountains, Antarctica: Columbus, Ohio, Ohio State University, Institute of Polar Studies Report 8, Research Foundation and the Institute of Polar Studies, 18 p.

_______ 1968, Glacial Geology of the Reedy Glacier Area, Antarctica: GSA Bulletin, v. 79, n. 4, p. 471–486, https://doi.org/10.1130/0016-7606(1968)79[471:GGOTRG]2.0.CO;2

Mukhopadhyay, S., Ackert, R. P., Jr., Pope, A. E., Pollard, D., and DeConto, R. M., 2012, Miocene to recent ice elevation variations from the interior of the West Antarctic ice sheet: Constraints from geologic observations, cosmogenic nuclides and ice sheet modeling: Earth and Planetary Science Letters, v. 337–338, p. 243–251, https://doi.org/10.1016/j.epsl.2012.05.015

Nichols, K. A., Goehring, B. M., Balco, G., Johnson, J. S., Hein, A. S., and Todd, C., 2019, New Last Glacial Maximum ice thickness constraints for the Weddell Sea Embayment: The Cryosphere, v. 13, p. 2935–2951, https://doi.org/10.5194/tc-13-2935-2019

Niedermann, S., 2002, Cosmic-Ray-Produced Noble Gases in terrestrial rocks: Dating tools for Surface Processes: Reviews in Mineralogy and Geochemistry, v. 47, n. 1, p. 731–784, https://doi.org/10.2138/rmg.2002.47.16

Niedermann, S., Graf, T., and Marti, K., 1993, Mass spectrometric identification of cosmic-ray-produced neon in terrestrial rocks with multiple neon components: Earth and Planetary Science Letters, v. 118, n. 1–4, p. 65–73, https://doi.org/10.1016/0012-821X(93)90159-7

Nishiizumi, K., 2004, Preparation of ^{26}Al AMS standards: Nuclear Instruments and Methods in Physics Research Section B: Beam Interactions with Materials and Atoms, v. 223–224, p. 388–392, https://doi.org/10.1016/j.nimb.2004.04.075

Nishiizumi, K., Imamura, M., Caffee, M. W., Southon, J. R., Finkel, R. C., and McAninch, J., 2007, Absolute calibration of ^{10}Be AMS standards: Nuclear Instruments and Methods in Physics Research Section B: Beam Interactions with Materials and Atoms, v. 258, n. 2, p. 403–413, https://doi.org/10.1016/j.nimb.2007.01.297

Parrenin, F., Dreyfus, G., Durand, G., Fujita, S., Gagliardini, O., Gillet, F., Jouzel, J., Kawamura, K., Lhomme, N., Masson-Delmotte, V., Ritz, C., Schwander, J., Shoji, H., Uemura, R., Watanabe, O., and Yoshida, N., 2007, 1-D-ice flow modelling at EPICA Dome C and Dome Fuji, East Antarctica: Climate of the Past, v. 3, p. 243–259, https://doi.org/10.5194/cp-3-243-2007

Phillips, W. M., McDonald, E. V., Reneau, S. L., and Poths, J., 1998, Dating soils and alluvium with cosmogenic ^{21}Ne depth profiles: Case studies from the Pajarito Plateau, New Mexico, USA: Earth and Planetary Science Letters, v. 160, n. 1–2, p. 209–223, https://doi.org/10.1016/S0012-821X(98)00076-4

Pollard, D., Chang, W., Haran, M., Applegate, P., and DeConto, R., 2016, Large ensemble modeling of the last deglacial retreat of the West Antarctic Ice Sheet: Comparison of simple and advanced statistical techniques: Geoscientific Model Development, v. 9, p. 1697–1723, https://doi.org/10.5194/gmd-9-1697-2016

Rocchi, S., LeMasurier, W. E., and Di, V. G., 2006, Oligocene to Holocene erosion and glacial history in Marie Byrd Land, West Antarctica, inferred from exhumation of the Dorrel Rock intrusive complex and from volcano morphologies: GSA Bulletin, v. 118, n. 7–8, p. 991–1005, https://doi.org/10.1130/B25675.1

Schäfer, J. M., Ivy-Ochs, S., Wieler, R., Leya, I., Baur, H., Denton, G. H., and Schlüchter, C., 1999, Cosmogenic noble gas studies in the oldest landscape on earth: Surface exposure ages of the Dry Valleys, Antarctica: Earth and Planetary Science Letters, v. 167, n. 3–4, p. 215–226, https://doi.org/10.1016/S0012-821X(99)00029-1

Shevenell, A. E., Kennett, J. P., and Lea, D. W., 2004, Middle Miocene Southern Ocean Cooling and Antarctic Cryosphere Expansion: Science, v. 305, n. 5691, p. 1766–1770, https://doi.org/15375266

Shuster, D. L., and Farley, K. A., 2005, Diffusion kinetics of proton-induced ^{21}Ne, ^{3}He, and ^{4}He in quartz: Geochimica et Cosmochimica Acta, v. 69, n. 9, p. 2349–2359, https://doi.org/10.1016/j.gca.2004.11.002

Spector, P., and Balco, G., 2020, Exposure-age data from across Antarctica reveal mid-Miocene establishment of polar desert climate: Geology, https://doi.org/10.1130/G47783.1

Spector, P., Stone, J., Pollard, D., Hillebrand, T., Lewis, C., and Gombiner, J., 2018, West Antarctic sites for subglacial drilling to test for past ice-sheet collapse: The Cryosphere Discussions, p. 1–26, https://doi.org/10.5194/tc-2018-88

Spector, P., Stone, J., and Goehring, B., 2019, Thickness of the divide and flank of the West Antarctic Ice Sheet through the last deglaciation: The Cryoshpere Discussions, https://doi.org/https://doi.org/10.5194/tc-2019-115

Steig, E. J., Fastook, J. L., Zweck, C., Goodwin, I. D., Licht, K. J., White, J. W. C., and Ackert, R. P., 2001, West Antarctic Ice Sheet Elevation Changes, *in* Alley, R. B., and Bindschadler, R. A., editors, The West Antarctic Ice Sheet-Behavior and Environment, v. 77, p. 75-90, https://doi.org/10.1029/AR077p0075

Stone, J. O., 2000, Air pressure and cosmogenic isotope production: Journal of Geophysical Research: Solid Earth, p. 23753–23759, https://doi.org/10.1029/2000JB900181

Stone, J., Spector, P., Hillebrand, T., Gombiner, J. H., Feathers, J. K., Talghader, J., Severinghaus, J. P., Pollard, D., Balco, G., and Fifield, L. K., 2019, West Antarctic Ice Sheet history from a subglacial bedrock core: San Francisco, California, Abstract C21E-1507 presented at 2019 Fall Meeting, American Geophysical Union, 10 Dec.

Sugden, D., and Denton, G., 2004, Cenozoic landscape evolution of the Convoy Range to Mackay Glacier area, Transantarctic Mountains: Onshore to offshore synthesis: GSA Bulletin, v. 116, n. 7–8, p. 840–857, https://doi.org/10.1130/B25356.1

Sugden, D. E., Hein, A. S., Woodward, J., Marrero, S. M., Rodés, Á., Dunning, S. A., Stuart, F. M., Freeman, S. P. H. T., Winter, K., and Westoby, M. J., 2017, The million-year evolution of the glacial trimline in the southernmost Ellsworth Mountains: Earth and Planetary Science Letters, v. 469, p. 42–52, https://doi.org/10.1016/j.epsl.2017.04.006

The Polar Rock Repository (PRR), Byrd Polar and Climate Research Center (BPCRC), Ohio State University, Polar rock and dredge samples available for research : and educational use from the PRR, https://doi.org/10.7289/V5RF5S18, Accessed May 10, 2020.

Vermeesch, P., Balco, G., Blard, P.-H., Dunai, T. J., Kober, F., Niedermann, S., Shuster, D. L., Strasky, S., Stuart, F. M., Wieler, R., and Zimmermann, L., 2015, Interlaboratory comparison of cosmogenic ^{21}Ne in quartz: Quaternary Geochronology, v. 26, p. 20–28, https://doi.org/10.1016/j.quageo.2012.11.009

Warny, S., Askin, R. A., Hannah, M. J., Mohr, B. A. R., Raine, J. I., Harwood, D. M., and Florindo, F., and the SMS Science Team, 2009, Palynomorphs from a sediment core reveal a sudden remarkably warm Antarctica during the middle Miocene: Geology, v. 37, n. 10, p. 955–958, https://doi.org/10.1130/G30139A.1

Webers, G., Craddock, C., Rogers, M., and Anderson, J., 1982, Geology of the Whitmore Mountains: International Union of Geological Sciences Publication, Series B, n. 4, Antarctic Geoscience, p. 841–847.

Wei, L. J., Raine, J. I., and Liu, X. H., 2014, Terrestrial palynomorphs of the Cenozoic Pagodroma Group, northern Prince Charles Mountains, East Antarctica: Antarctic Science, v. 26, n. 1, p. 69–79, https://doi.org/10.1017/S0954102013000278

Zachos, J., Pagani, M., Sloan, L., Thomas, E., and Billups, K., 2001, Trends, Rhythms, and Aberrations in Global Climate 65 Ma to Present: Science, v. 292, n. 5517, p. 686–693, https://doi.org/11326091